Rest-frame UV and optical emission line diagnostics of ionized gas properties: a test case in a star-forming knot of a lensed galaxy at $z \sim 1.7$

Ayan Acharyya [ID],[1,2]★ Lisa J. Kewley,[1,2] Jane R. Rigby,[3] Matthew Bayliss,[4] Fuyan Bian,[1,5] David Nicholls,[1] Christoph Federrath,[1,2] Melanie Kaasinen [ID],[6] Michael Florian[3] and Guillermo A. Blanc[7,8]

[1]*Research School of Astronomy and Astrophysics, Australian National University, Canberra, ACT 2611, Australia*
[2]*ARC Centre of Excellence for All Sky Astrophysics in 3 Dimensions (ASTRO 3D), Canberra, ACT 2611, Australia*
[3]*Astrophysics Science Division, Goddard Space Flight Center, 8800 Greenbelt Rd., Greenbelt, MD 20771, USA*
[4]*MIT Kavli Institute for Astrophysics and Space Research, 77 Massachusetts Ave., Cambridge, MA 02139, USA*
[5]*European Southern Observatory, Alonso de Córdova 3107, Vitacura, Santiago 19, Casilla 19001, Chile*
[6]*Max Planck Institute für Astronomie, Königstuhl 17, D-69117 Heidelberg, Germany*
[7]*Observatories of the Carnegie Institution for Science, 813 Santa Barbara Street, Pasadena, CA 91101, USA*
[8]*Departamento de Astronomía, Universidad de Chile, Camino del Observatorio 1515, Las Condes, Santiago, Chile*

ABSTRACT

We examine the diagnostic power of rest-frame ultraviolet (UV) nebular emission lines, and compare them to more commonly used rest-frame optical emission lines, using the test case of a single star-forming knot of the bright lensed galaxy RCSGA 032727–132609 at redshift $z \sim 1.7$. This galaxy has complete coverage of all the major rest-frame UV and optical emission lines from Magellan/MagE and Keck/NIRSPEC. Using the full suite of diagnostic lines, we infer the physical properties: nebular electron temperature (T_e), electron density (n_e), oxygen abundance (log (O/H), ionization parameter [log (q), and interstellar medium (ISM) pressure (log (P/k)]. We examine the effectiveness of the different UV, optical, and joint UV–optical spectra in constraining the physical conditions. Using UV lines alone we can reliably estimate log (q), but the same is difficult for log (O/H). UV lines yield a higher (~ 1.5 dex) log (P/k) than the optical lines, as the former probes a further inner nebular region than the latter. For this comparison, we extend the existing Bayesian inference code IZI, adding to it the capability to infer ISM pressure simultaneously with metallicity and ionization parameter. This work anticipates future rest-frame UV spectral data sets from the James Webb Space Telescope (*JWST*) at high redshift and from the Extremely Large Telescope (ELT) at moderate redshift.

Key words: ISM: evolution – galaxies: abundances – ultraviolet: ISM.

1 INTRODUCTION

Understanding the evolution of interstellar medium (ISM) properties requires measuring galaxies at both lower redshifts ($z \leq 1$) where the star formation has been quenched due to feedback from several physical processes (e.g. Bluck et al. 2014; Cicone et al. 2014; Leslie et al. 2016; Schwamb et al. 2016) including turbulence (e.g. Federrath & Klessen 2012; Federrath et al. 2017; Zhou et al. 2017), and at higher redshifts ($z \sim 2$) where the star formation rate (SFR) is at its peak (e.g. Kulas, Shapley & Hainline 2010; Kewley et al. 2016; Uzgil et al. 2016).

The star formation history (e.g. Schulte-Ladbeck et al. 2003), ISM conditions (e.g. Lamareille et al. 2004; Tremonti et al. 2004;

Gallazzi et al. 2005; Contursi et al. 2017) and kinematics (e.g. Cicone, Maiolino & Marconi 2016) of low-redshift galaxies have been studied extensively thanks to large, targeted surveys (e.g. Ho et al. 2016; Belfiore et al. 2017; Ellison et al. 2018; Medling et al. 2018). Not only are low-z galaxies brighter then the distant ones, but also in many cases we have spatially resolved properties. In contrast, the physical conditions of high-z ($z > 1$) galaxies are still poorly understood, because these galaxies are fainter and harder to observe. Spatially resolved studies of high-z galaxies are difficult with current telescopes and the resolution is poorer than for the local samples (e.g. Förster Schreiber et al. 2009; Wisnioski et al. 2015). The advent of the next generation of large ground-based [Giant Magellan Telescope, GMT (Johns 2004); Extremely Large Telescope, ELT (Sanders 2013); Thirty Metre Telescope, TMT (Hook 2009)] and space-based telescopes [*James Webb Space Telescope*, *JWST* (Gardner et al. 2006)] will facilitate spectroscopic

★ E-mail: ayan.acharyya@anu.edu.au

observations of galaxies with unprecedented spatial resolution ($\sim$0.1 arcsec), out to very high redshifts ($z \sim$ 6–10) and detection of the first generation of galaxies ($z \sim$ 15).

JWST will be able to observe the rest-frame optical emission lines in a multiplexed way with its NIRSpec instrument for galaxies at $z \leq 6.4$. Moreover, for $z \geq 3$ *JWST* can additionally capture diagnostic rest-frame UV lines. At moderate redshifts ($z \geq 3$) *JWST* /NIRSpec will be able to capture both rest-frame optical and rest-frame UV diagnostics. At higher redshifts ($z \geq 6.4$), the rest-frame optical lines redshift out of the NIRSpec bandpass and are no longer accessible for multiplexed spectroscopy, though they can be captured singly by the MIRI (Mid-Infrared Instrument Instrument). For the highest redshift ($7 < z < 10$) galaxies, all *JWST* may spectroscopically detect are the rest-frame UV lines. This motivates the development of a suite of UV emission line diagnostics, as well as a full UV+optical suite of diagnostics to be used at moderate redshifts.

Even prior to the onset of the next-generation telescopes, we can preview the measurements that will be possible with such facilities by studying galaxies that are strongly magnified through lensing. Gravitational lensing has been used by astronomers to quantify the ISM conditions in galaxies at $z \geq 1.5$ (e.g. Rigby 2009; Yuan & Kewley 2009; Bian et al. 2010; Rigby et al. 2011; Jones et al. 2013; Yuan, Kewley & Richard 2013; Bayliss et al. 2014; Cañameras et al. 2015; Jones, Martin & Cooper 2015; Leethochawalit et al. 2016; Wang et al. 2017; James et al. 2018). In addition to magnifying background galaxies, gravitational lensing stretches the images of the galaxies into extended arcs, making it possible to spatially resolve individual star-forming knots (fig. 1 of Bayliss et al. 2014; Cañameras et al. 2015; Swinbank et al. 2015; Sharda et al. 2018).

Diagnostics using rest-frame optical nebular lines have been extensively applied to H II regions and galaxies (e.g. Pagel et al. 1979; McGaugh 1991; Zaritsky, Kennicutt & Huchra 1994; Kewley et al. 2001; Kewley & Dopita 2002; Kobulnicky & Kewley 2004; Pettini & Pagel 2004; Sanders et al. 2016a, henceforth KD02, KK04, PP04). UV diagnostics appear promising (e.g. Garnett et al. 1995a,b; Izotov et al. 2006b; Stark et al. 2014; Feltre, Charlot & Gutkin 2016; Jaskot & Ravindranath 2016; Byler et al. 2018, henceforth I06, G95a, and G95b, respectively) but have not yet been extensively tested. Moreover, the atomic data and stellar atmospheric libraries used for the calibrations of the earlier works have now been updated. These updates affect the suite of UV and optical diagnostics developed to date.

Recent studies have presented improvements to the rest-frame UV and optical diagnostics. Kewley et al. (2019a, hereafter K19a) present a set of rest-frame optical and UV line diagnostics for electron density and ISM pressure using the updated version of the MAPPINGS photoionzation models (Sutherland et al. 2013) (explained in Section 5.2). Using these models, Kewley, Nicholls & Sutherland (2019b, hereafter K19b) further present a set of optical and UV diagnostics for ionization parameter and metallicity. Nicholls et al. (in preparation; N18 hereafter) propose new methods for determining the nebular electron temperature using rest-frame UV oxygen emission lines combined with improved theoretical models. Dopita et al. (2016, hereafter D16) present a robust technique to isolate the dependence of oxygen abundance on a set of nebular optical lines (independent of ionization parameter and ISM pressure) applicable for high-z ($z \sim 2$) galaxies. These new diagnostics, together with the existing diagnostics, constitute a comprehensive suite that can be employed to determine ISM properties of high-z galaxies. However, the new diagnostics have not yet been tested using observations of galaxies.

In addition to strong emission line diagnostics (SEL), Bayesian techniques are also becoming increasingly important in inferring ionized gas properties due to their ability to probe asymmetry and non-trivial topography in the probability distributions of the properties. Recent Bayesian estimation tools like IZI (Blanc et al. 2015), BOND (Vale Asari et al. 2016), HII-CHI-mistry (Pérez-Montero 2015), and NebulaBayes (Thomas et al. 2018) have proven useful in inferring nebular gas properties. However, in light of the recent development of SEL diagnostics, particularly the rest-frame UV diagnostics, it is necessary to test the agreement between the Bayesian and SEL techniques. Hence, in this work we compare the SEL diagnostics with a new, extended version of IZI, as described later in Section 6.

The purpose of this paper is to test these new diagnostics by applying them to a star-forming knot of a $z \sim 2$ galaxy with full coverage of these diagnostic lines. Herein we exploit the advantage that spatially resolved spectroscopy has over other high-z samples. Choosing a single star-forming knot of the lensed galaxy RCS0327 for the testing allows us to probe a small ($\sim$100 pc) spatial region, which can be expected to have fairly homogeneous ISM properties with high fraction of H II region relative to diffuse gas.

This paper is organized as follows. In Section 2 we justify the selection of a single star-forming knot of RCS0327 as the test case and describe the selection of the local galaxies used for comparison. Section 3 describes the observation and data reduction for both the Keck/NIRSPEC and Magellan/MagE data. We explain the tools used for our analysis, including line fitting algorithms, various diagnostics used, and the results obtained from them in Section 5. The comparison among various results is discussed in Section 7 followed by a summary of our work in Section 8.

We use a solar oxygen abundance $12 + \log(\text{O/H}) = 8.72$ (Asplund et al. 2009) throughout the paper. We assume a standard flat Λ cold dark matter cosmology with $H_0 = 70$ km s^{-1} Mpc^{-1} and matter density $\Omega_M = 0.27$. For the emission lines, we adopt the sign convention of negative equivalent width and use the wavelengths from the NIST data base, the Leitherer et al. (2011) atlas, and MAPPINGS v5.

2 SAMPLE SELECTION

The primary limitation in the development of rest-frame UV spectral diagnostics has been the lack of high-quality spectra. Project MEGaSaURA (Rigby et al. 2018) has obtained high signal to noise, moderate spectral resolution ($R \sim 3000$) spectra for 15 bright gravitationally lensed galaxies. From that sample, we select the spectrum of knot-E of RCS0327 (henceforth referred to as RCS0327-E) for our pilot study, for the following reasons:

(i) RCSGA 032727–132609 (henceforth RCS0327) is a very bright lensed galaxy with an r-band magnitude of 19.1 (Wuyts et al. 2010; Sharon et al. 2012).

(ii) The fact that the lensed galaxy appears as a very extended (38 arcsec) arc makes it possible to resolve and target individual star-forming knots. Spectra of four knots have been published; we select knot-E (see Sharon et al. 2012, fig. 1) for our analysis in this paper because it has the highest signal-to-noise ratio (SNR).

(iii) The spectrum of RCS0327 has an SNR per resolution element $\sim$20 at $\lambda_{\text{obs}} = 5000$ Å, sufficient to clearly detect the rest-frame UV emission lines.

(iv) Rest-frame optical spectra for this object have been obtained from Keck/NIRSPEC (Rigby et al. 2011, henceforth R11), Keck/OSIRIS (Wuyts et al. 2014b), and *HST*/WFC3 G141 grism

(hereafter W14; Whitaker et al. 2014). Wuyts et al. (2014b) also report optical fluxes for knots B, U from Magellan/FIRE observations and that for knot U from re-extracted Keck/NIRSPEC observations. W14 report grism fluxes from several other star-forming knots too. However, the largest number of optical+UV emission lines are detected in Knot E, which allow us to compare the extensively used optical diagnostics to the new UV diagnostics.

RCS0327 was first discovered (Wuyts et al. 2010) in a dedicated search for highly magnified giant arcs (Bayliss 2012) in the Red Sequence Cluster Survey 2 (RCS2; Gilbank et al. 2011). Sharon et al. (2012) performed a source plane reconstruction of RCS0327, based on *HST*/WFC3 imaging data, down to a scale of ∼100 pc. Due to its apparent brightness, this galaxy has been subjected to extensive subsequent spectroscopic analyses. R11 constrained the nebular physical properties of RCS0327 using the spatially summed Keck/NIRSPEC (rest-frame optical) spectra. Wuyts et al. (2014a) studied the stellar populations and concluded that RCS0327 is a starburst galaxy (SFR 30–50 $M_\odot$ yr^{-1}; Wuyts et al. 2012a) with a young (5–100 Myr; Wuyts et al. 2014a) stellar population that has just started to build-up its stellar mass (10^7–5×10^8 $M_\odot$; Wuyts et al. 2014a). W14 analysed spatial variations in *HST*/WFC3 grism spectra of RCS0327 and reported no appreciable knot-to-knot variation in reddening, and an enhanced SFR (∼2 dex above the star formation main sequence) due to an ongoing interaction. They also found spectroscopic evidence of the presence of O stars in most knots (except knots E and F which have lower He I/Hβ ratios), which is consistent with the young stellar population scenario. Bordoloi et al. (2016) examined the galactic outflows for this galaxy as traced by the Mg II and Fe II emission and its spatial variation, finding large outflow velocities (∼170–250 km s^{-1}) and mass outflow rates ($\gtrsim$30–50 $M_\odot$ yr^{-1}). However, Rigby et al. (2014) report a lack of correlation between the Mg II and Lyα emissions, which implies that the source of Mg II emission is not nebular, but may instead be resonantly scattered continuum. Overall, the picture that has emerged is that RCS0327 hosts a young stellar population that is driving a large-scale outflow.

In this work, we analyse the spectra of one particular knot of star formation (knot E) within RCS0327. A unique feature of this analysis is that the spectra cover an ∼100 pc (Sharon et al. 2012) star-forming region [classified using the Baldwin, Phillips & Terlevich (BPT) diagram and KD02 line]. Our work has the distinct advantage in that the physical conditions can be expected to be fairly homogeneous within the small (∼100 pc) spatial region that the spectra probe, rather than being averaged across several kiloparsecs, which ensures fair comparison to photoionization models. Moreover, the relative contribution from H II regions with respect to diffuse ionized gas is expected to be very high because we integrate over a small star-forming knot, rather than the whole galaxy.

We compare the rest-frame UV and rest-frame optical emission line fluxes to newly developed diagnostics (K19a,b; N18), to constrain the ionization parameter ($\log(q)$), electron density (n_e), ISM pressure ($\log(P/k)$), electron temperature (T_e), and oxygen abundance ($12 + \log(O/H)$). We also consider how the results would differ if we had only the UV data set, or only the optical data set, using a Bayesian approach (detailed in Section 6). Moreover, given that the [O II] $\lambda\lambda3727,9$ doublet will be within the wavelength coverage of *JWST* up to $z \sim 12$, we also investigate the effect of including the [O II] $\lambda\lambda3727,9$ lines with the set of rest-frame UV emission lines.

3 OBSERVATIONS

We use the rest-frame optical spectra from the NIRSPEC instrument on Keck and rest-frame ultraviolet spectra from the MagE instrument on Magellan.

3.1 Rest-frame optical spectroscopy from NIRSPEC on Keck

Near-infrared spectra of RCS0327-E, covering the rest-frame optical, were obtained on UT 2010 Feb. 4 with the NIRSPEC spectrograph (McLean et al. 1998) on the Keck II telescope. The spectra were originally published in R11, along with a detailed description of the observation and data reduction procedures. Since only a basic lensing model was available at that time, the spectrum in the long-slit was summed across the spatial direction. Subsequently, high-resolution images with the *Hubble Space Telescope* (*HST*) revealed that the NIRSPEC observations had captured multiple physically distinct knots of star formation (see Sharon et al. 2012, fig. 6), the brightest of which they labelled Knot E and Knot U. Guided by the *HST*-enabled lensing model, Wuyts et al. (2014b) re-extracted the spectra, producing spectra for these two physical regions. Subsequently, W14 improved the measurement of the reddening for RCS0327. Therefore, we take the NIRSPEC line fluxes reported for Knot E by Wuyts et al. (2014b), and apply the reddening of $E(B - V)_{\text{gas}} = 0.40 \pm 0.07$ measured by W14, to compute updated cross-filter scaling factors, as we describe in more detail in Section 4.1.

3.2 Rest-frame UV spectroscopy from MagE on Magellan

Optical spectra of RCS0327-E (see Sharon et al. 2012, fig. 1), covering the rest-frame ultraviolet, were obtained on multiple nights in the range UT 2008-07-31 to UT 2010-12-10 with the MagE instrument (Marshall et al. 2008) on the Magellan Clay telescope. The observations and data reduction are described in Rigby et al. (2018). The data were reduced using the MagE pipeline, which is part of the Carnegie PYTHON Distribution.[1] The full spectra from each observation were obtained by combining the weighted average of different spectral orders. Observations from different nights were then combined via a weighted average to obtain the resulting rest-frame UV spectra of RCS0327-E used in this paper. The spectra were flux-calibrated by comparing to spectrophotometric standard stars, as described in Rigby et al. (2018). The spectra were corrected for Milky Way reddening. The effective spectral resolution of the final combined spectrum, measured from the widths of night sky lines, is $R = 3650 \pm 120$ (median and absolute median deviation).

4 FLUX MEASUREMENTS

4.1 Keck/NIRSPEC spectral line fits

For each NIRSPEC filter setting (N1, N3, and N6, roughly corresponding to *J* band, *H* band, and *Ks* band, respectively), all emission lines were fit simultaneously with Gaussian profiles by Wuyts et al. (2014b, see their sections 2.3 and 2.4). Relative flux offsets are expected in the NIRSPEC spectra across the three grating settings, due to slit losses associated with variable seeing. As a result, the fluxes of the NIRSPEC-1 and NIRSPEC-6 spectra had to be adjusted with respect to the flux calibration in NIRSPEC-3. Section 3.2 of

---

[1]http://code.obs.carnegiescience.edu

R11 describes how the Balmer lines were used to perform this process, using the at-the-time best measurement of reddening, $E(B - V)_{gas} = 0.23 \pm 0.23$. This procedure produced offset factors of 1.15 for N1 and 0.61 for N6, both with respect to N3.

4.2 Magellan/MagE spectral line fits

We fit the continuum with an automatic routine that masks the positions of all expected spectral features, including from known intervening absorption systems, and then apply boxcar smoothing. The result is almost identical to the hand-fit spline continuum described in Rigby et al. (2018). We subsequently fit the emission lines in the combined, continuum normalized spectrum using a *Python*-based, automated line fitting code, explained below.

We simultaneously fit all neighbouring spectral lines with one Gaussian profile per line employing the PYTHON tool `scipy.optimize.curve_fit` that implements the non-linear least-squares method. A neighbour is defined as follows. Each line centroid is assumed to have a window of ± 5 spectral resolution elements, both blueward and redward. If the windows of any two adjacent lines overlap they are neighbours. A neighbour of a neighbour is considered in the same group of lines, which are fit simultaneously. As an example, if there are 4 lines with separation between each adjacent pair of line centroids less than ± 10 resolution elements (5 resolution elements from the window of each line), the lines are considered as a single group. This group is fit with a quadruple Gaussian function with $4 \times 3 = 12$ parameters, where the parameters are height, width, and centroid of the Gaussians for each line in the group. We set the continuum value to unity[2] because, in this case, we use a continuum normalized spectrum. Initially, the nebular redshift is measured by fitting the strongest emission lines (for RCS0327-E it is the [C III]$\lambda\lambda$1906,8 doublet) with sufficiently large allowance for the fitted redshift. Subsequently, an initial guess for each line centroid λ_{in} is provided to `curve_fit()` by redshifting the rest-frame vacuum wavelengths by the nebular redshift. The centroids are forced to be fit within a window of $\lambda_{in} \pm 3\sigma$ wavelength interval corresponding to the uncertainties in the nebular redshift. The line width is fit within upper and lower bounds of $300\,km\,s^{-1}$ and one spectral resolution element, respectively. The amplitude of the Gaussians was allowed to vary freely. We measure rest-frame equivalent widths (W_r) from both the fitted Gaussian parameters and by direct summation. In this paper, we quote the W_r values derived using the former method.

In order to determine the significance of the W_r measurements ($W_{r,signi}$), we define a quantity $W_{r,Schneider}$ as the W_r derived by interpolating a rolling average of the error weighted W_r at every point throughout the spectrum, following Schneider et al. (1993, section 6.2). The $W_{r,signi}$ is then defined as the ratio of the measured W_r of a line to the $W_{r,Schneider}$ computed at the line centre. The rolling average technique gives us a quantifiable estimate of the spectral noise. We consider all lines that meet the criteria (a) $W_{r,signi} > 3$, and (b) SNR > 1, to be detected.[3] Features not satisfying these criteria are considered to be non-detections, for which we quote $3 \times W_{r,Schneider}$ as the 3σ upper limits of W_rs. We repeat the same operation on measured line flux values (f) to derive $f_{Schneider}$, f_{signi}, and f_{uplim}. In the absence of flux (f), we translate f_{uplim} to

---

[2]The code is capable of fitting the continuum value, for each group, as an additional parameter if desired.

[3]There are cases where only criteria (a) is satisfied, especially when the code fits a broad emission in the noisy part of the spectrum.

Table 1. Keck/NIRSPEC line flux measurements. These measurements include updated (relative to Wuyts et al. 2014b) tweak factors to take into account the cross-filter flux calibration. Flux$_{obs}$ and δ flux$_{obs}$ denote the observed flux and uncertainty, respectively. Flux$_{dereddened}$ is the dereddened flux using $E(B - V) = 0.4 \pm 0.07$. All fluxes and uncertainties are in units of $10^{-17}\,erg\,s^{-1}\,cm^{-2}$.

Line ID	λ_{rest} (Å)	Flux$_{obs}$	δ flux$_{obs}$	Flux$_{dereddened}$
		Filter N1		
[O II] 3727,9	3728.483	165.3	7.3	958.36
[O II] 3727	3727.092	87.8	3	509.23
[O II] 3729	3729.875	76.6	4	443.94
[Ne III] 3869	3869.860	25.4	2.6	141.33
		Filter N2		
Hζ	3890.166	17.8	2	98.408
Hδ	3971.198	16	4.1	86.09
Hϵ	4102.892	7	3	35.882
		Filter N3		
Hγ	4341.692	49.8	2	231.64
O III 4363	4364.435	5.5	2	25.34
[Ar IV] 4741	4741.449	0	0	0
Hβ	4862.691	119	1.6	449.53
[O III] 4959	4959.895	190	1.4	693.78
[O III] 5007	5008.239	613	3	2202.5
Hα	6564.632	465.2	23.2	1183.4
[N II] 6584	6585.273	55	3.9	139.4
[S II] 6717	6718.294	26.3	2.3	65.114
S II 6731	6732.674	19.4	6.2	47.91
[Ar III] 7136	7137.770	10.8	3.1	24.824

lower/upper limits on line ratios and consequently to limits on the ISM properties. We present the adjusted fluxes in Table 1.

We present the emission line fluxes and upper limits of nebular lines in the MagE spectrum in Table 2 and show the Gaussian fits to the MagE data in Figs 1 and 2. Some of the emission lines of interest in our spectrum are affected by intervening absorption lines. We fit the intervening lines simultaneously with the emission lines, to properly account for the missing (absorbed) emission line fluxes (e.g. see bottom-left panel of Fig. 1). The intervening absorption features, along with their strengths and redshifts are presented in Table 3. These intervening lines have been studied by Lopez et al. (2018).

5 STRONG EMISSION LINE DIAGNOSTICS

W14 measured a luminosity-weighted average reddening value of $E(B - V) = 0.4 \pm 0.07$. We use the W14 $E(B - V)$ value and Cardelli, Clayton & Mathis (1989) reddening law to correct the NIRSPEC and MagE fluxes for extinction. The quoted uncertainties in the measured fluxes are inferred directly from the Gaussian fits to the emission lines. To obtain the dereddened flux uncertainty, we scale the measured flux uncertainty with the same dereddening factor as applied to the flux measurements. We take into account the uncertainties in both the dereddened flux and the $E(B - V)$ via a Monte Carlo approach, as described in Section 5.1.

We list the emission line ratios used and corresponding labels for all the diagnostics used in Table 4. The following sections describe the diagnostics used. Fig. 3 shows the results and Table 5 quotes the corresponding values.

Line ID	λ_{rest} (Å)	$W_{r,fit}$ (Å)	$\delta W_{r,fit}$ (Å)	$W_{r,signi}$ (Å)	Flux$_{obs}$ (10^{-17} ergs s^{-1} cm^{-2})	δ flux$_{obs}$ (10^{-17} ergs s^{-1} cm^{-2})	Flux$_{dereddened}$ (10^{-17} ergs s^{-1} cm^{-2})
Lyα	1215.6700	> -0.5706	–	–	<0.43	–	<23.32
O I 1304	1304.8576	> -0.2609	–	–	<0.25	–	<5.26
O I 1306	1306.0286	> -0.2589	–	–	<0.24	–	<5.22
Si II 1309	1309.2757	-0.6397	0.15	7.37	1.62	0.37	34.82
C II 1335a	1334.5770	> -0.1547	–	–	<0.15	–	<3.16
C II 1335b	1335.6630	> -0.1575	–	–	<0.15	–	<3.22
C II 1335c	1335.7080	> -0.1575	–	–	<0.15	–	<3.22
N II] 1430	1430.4100	> -0.1131	–	–	<0.10	–	<2.21
N II] 1431	1430.9730	> -0.116	–	–	<0.11	–	<2.26
N IV] 1486	1486.5000	-0.2242	0.09	5.92	0.55	0.23	11.17
Si II 1533	1533.4312	-0.3645	0.05	10.83	0.86	0.12	16.84
He II 1640	1640.4170	-0.4451	0.07	15.06	1.03	0.16	18.56
O III] 1660	1660.8090	-0.1209	0.07	4.24	0.28	0.16	4.94
O III] 1666	1666.1500	-0.4817	0.07	15.88	1.10	0.16	19.52
N III] 1750	1749.7000	-0.3396	0.05	13.45	0.73	0.11	12.82
[Si II] 1808	1808.0130	> -0.0896	–	–	<0.07	–	<1.22
[Si II] 1816	1816.9280	-0.3036	0.06	9.83	0.62	0.13	11.14
[Si III] 1882	1882.7070	-0.3104	0.05	11.59	0.61	0.10	11.75
Si III] 1892	1892.0290	-0.4239	0.06	15.22	0.82	0.12	16.10
[C III] 1906	1906.6800	-1.5011	0.32	52.55	2.89	0.61	57.99
C III] 1908	1908.7300	-1.1148	0.11	38.19	2.14	0.21	43.16
N II] 2140	2139.6800	> -0.1038	–	–	<0.06	–	<2.24
[O III] 2320	2321.6640	> -0.1132	–	–	<0.06	–	<1.39
C II] 2323	2324.2140	> -0.1023	–	–	<0.05	–	<1.24
C II] 2325c	2326.1130	-0.7885	0.20	13.72	1.08	0.27	25.58
C II] 2325d	2327.6450	-0.3731	0.10	10.39	0.51	0.13	12.01
C II] 2328	2328.8380	-0.1435	0.08	4.10	0.20	0.11	4.59
Si II] 2335a	2335.1230	> -0.1064	–	–	<0.05	–	<1.22
Si II] 2335b	2335.3210	> -0.1064	–	–	<0.05	–	<1.22
Fe II 2365	2365.5520	-0.5465	0.07	14.59	0.71	0.10	14.68
Fe II 2396a	2396.1497	> -0.1234	–	–	<0.06	–	<1.07
Fe II 2396b	2396.3559	> -0.1279	–	–	<0.06	–	<1.11
[O II] 2470	2471.0270	-0.9819	0.07	25.09	1.20	0.08	18.01
Fe II 2599	2599.1465	> -0.1064	–	–	<0.04	–	<0.50
Fe II 2607	2607.8664	> -0.1694	–	–	<0.07	–	<0.77
Fe II 2612	2612.6542	-0.732	0.20	16.06	0.77	0.21	8.89
Fe II 2614	2614.6051	> -0.1453	–	–	<0.06	–	<0.65
Fe II 2618	2618.3991	> -0.1384	–	–	<0.05	–	<0.61
Fe II 2621	2621.1912	> -0.1351	–	–	<0.05	–	<0.59
Fe II 2622	2622.4518	> -0.1569	–	–	<0.06	–	<0.69
Fe II 2626	2626.4511	-0.9937	0.10	21.09	1.04	0.11	11.67
Fe II 2629	2629.0777	> -0.1376	–	–	<0.05	–	<0.59
Fe II 2631	2631.8321	> -0.1259	–	–	<0.05	–	<0.54
Fe II 2632	2632.1081	> -0.1245	–	–	<0.05	–	<0.53
Mg II 2797b	2798.7550	-1.089	0.07	23.33	1.08	0.07	10.00
Mg II 2797d	2803.5310	-0.4567	0.06	10.97	0.45	0.06	4.19
He I 2945	2945.1030	> -0.1515	–	–	<0.07	–	<0.55

5.1 Deriving uncertainties

For each emission line involved in a particular diagnostic, we randomly draw a flux value from a Gaussian distribution which has a mean equal to the measured (non-dereddened) flux and a width equal to the 1σ uncertainty in the measurement. We also randomly draw a value of $E(B - V)$ from the measured range of 0.4 ± 0.07. Then we deredden the fluxes relative to the reddest line involved in that particular diagnostic, using the randomly drawn $E(B - V)$ for that particular iteration. For instance, if the diagnostic involves the [O III] $\lambda\lambda$ 4959,5007/[O III] λ 4363 ratio, we de-redden the [O III] λ

4363 and [O III] λ 4959 fluxes to bring them to the reference frame of the [O III] λ 5007 line. Because only the line ratios are relevant for our purposes, and not the overall shape of the spectrum, the relative de-reddening is performed to ensure that we are not overestimating the de-reddening uncertainties. We calculate all the diagnostics, explained in the preceding sections, with this set of de-reddened line fluxes and repeat the process 10^4 times. This leaves us with 10^4 different values of each parameter we are trying to estimate, which we convert to a probability distribution function (PDF). We quote the median values of each distribution, along with the 16th and
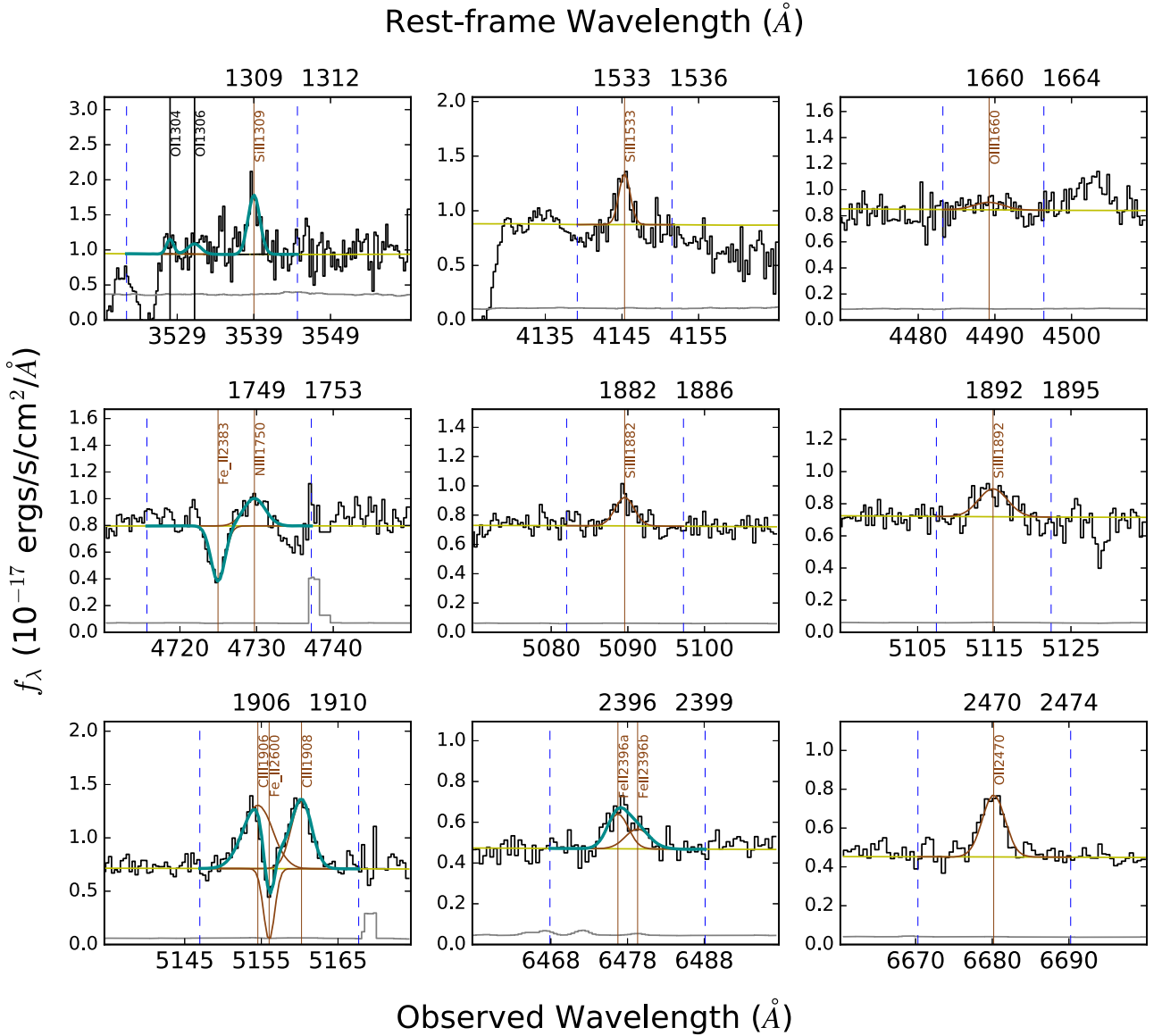
Figure 1. Gaussian fits to the MagE spectra for individual lines. The black line is the observed spectrum, whereas grey and yellow denote the 1σ uncertainty spectrum and the continuum, respectively. Brown solid lines represent the Gaussian fit of individual lines. Thick dark cyan lines are the sum of the Gaussian fits, wherever there are multiple lines. The fitting routine works on a portion of the spectrum as shown bounded by blue dashed lines. The fitted value of the central wavelength is denoted by a vertical brown solid line, if the line is detected (i.e. $>3\sigma$) and by a black line if not (i.e. $<3\sigma$). A single Gaussian is fit to a single line or multiple Gaussians are simultaneously fit to a group of lines, depending on the separation between neighbouring lines. This is visible, for example, in the C III] 1906–1908 doublet fitting.

84th percentiles as the 1σ lower and upper limits of that parameter. To calculate the mean value and uncertainties of a quantity from multiple SEL diagnostics, we simply add the PDFs from the concerned diagnostics and then quote the 50th, 16th, and 84th percentiles of the summed PDF. We adopt this approach to account for asymmetry (non-Gaussianity) in the uncertainties of physical parameters, which indeed is the case for some of the properties.

5.2 Rest-frame optical diagnostics

We use the nebular [O II] $\lambda\lambda$ 3727,3729, [O III] $\lambda\lambda$ 4959,5007, [O III] λ 4363, [N II] λ 6583, and [S II] $\lambda\lambda$ 6716, 6731 lines from the rest-frame optical NIRSPEC spectrum (Table 1) to determine the physical quantities in RCS0327-E.

5.2.1 Electron temperature

We measure the electron temperature (T_e), in the [O III] nebular zone, using the [O III] $\lambda\lambda$4959,5007/[O III] λ4363 ratio, following equations (1) and (2) of I06, iteratively. This method has almost no dependence on the n_e, determined using [S II] line fluxes, and can therefore constrain T_e even in absence of the [S II] lines. The [O III] $\lambda\lambda$ 4959,5007 and [O III] λ4363 emission lines originate from the $^1S \rightarrow {}^1D$ and $^1D \rightarrow {}^3P$ transitions, which can be completely constrained by atomic physics from a given T_e. Therefore, the [O III] $\lambda\lambda$ 4959,5007/[O III] λ4363 ratio is an excellent T_e diagnostic in the low-density ($n_e < 10^5$ cm^{-3}) regime. Using the I06 diagnostic we derive $T_e = 1.22^{+0.16}_{-0.17} \times 10^4$ K.

We also use the [O III] λ4363/[O III] λ5007 ratio calibration from N18 and which also yields $T_e = 1.22^{+0.16}_{-0.17} \times 10^4$ K. The N18
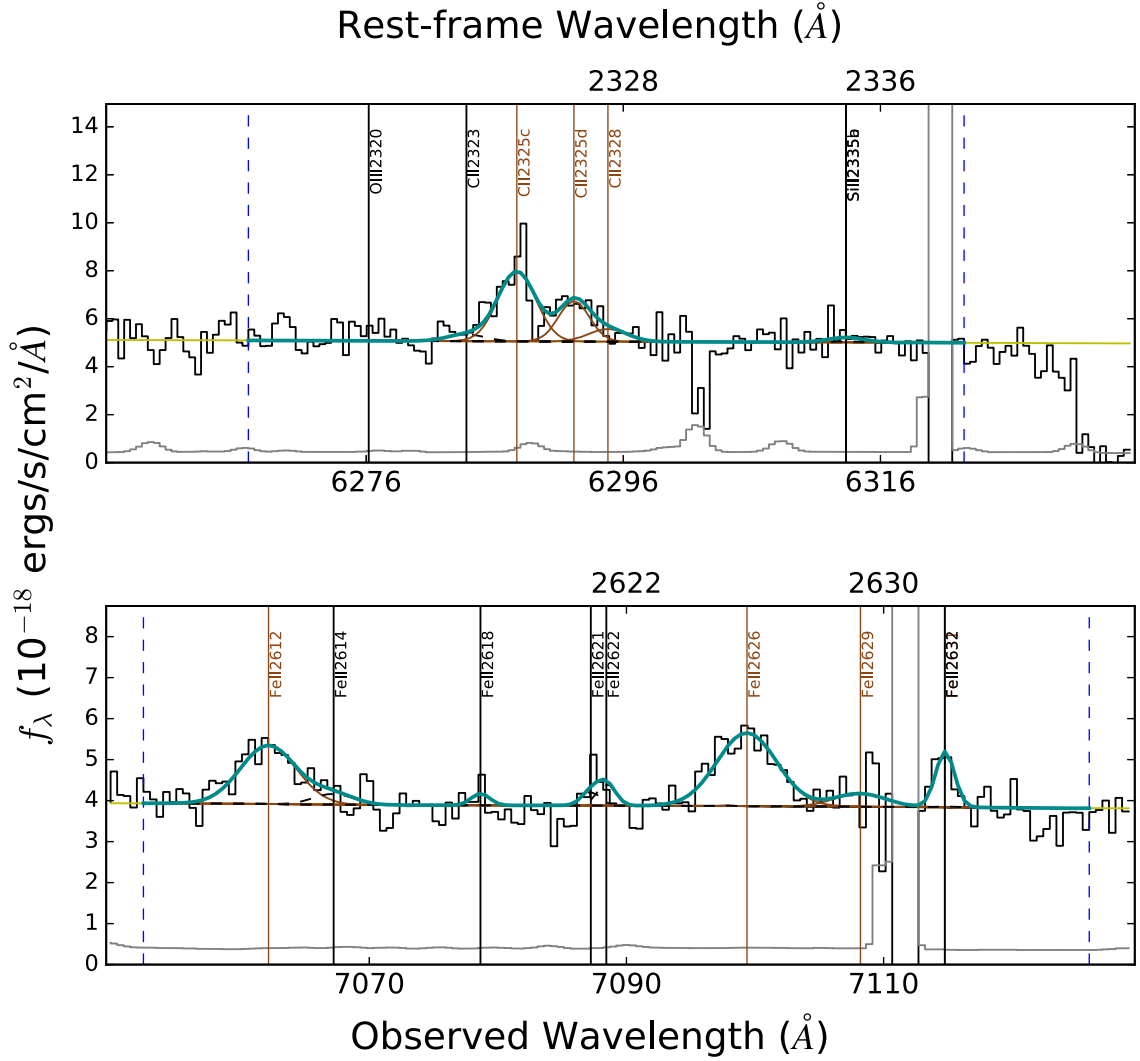
Figure 2. Our fits of the C II] 2323 (top) and Fe II 2600 (bottom) complex. The colour coding is as in Fig. 1. There are $>3\sigma$ detections for only some of the lines (brown vertical lines) in this complex. For the rest (black vertical lines) we quote upper limits in Table 2. Blue solid lines indicate the initial guess/es of the line centre/s provided to the fitting code. For each line/group, only the portion bounded by blue dashed lines is fit.

Table 3. Intervening absorption lines in RCS0327-EMagellan/MagE spectrum. $W_{r,fit}$ denotes the rest-frame equivalent width measured, in Å. z an Δz are the redshift and corresponding uncertainty, respectively, as measured from our line fitting code.

Line ID	λ_{rest} (Å)	$W_{r,fit}$ (Å)	$\delta W_{r,fit}$ (Å)	zz	zz_u
Fe II 2344	2344.2140	0.4791	0.0612	0.982 85	0.000 06
Fe II 2383	2382.7650	0.5997	0.0578	0.982 98	0.000 04
Al II 1670	1670.7874	0.0572	0.0609	1.878 80	0.001 50
Fe II 2586	2586.6500	0.3040	0.0456	0.982 90	0.000 04
Fe II 2600	2600.1729	0.8633	0.3090	0.982 95	0.000 03
Mg II 2796	2796.3520	1.0939	0.0671	0.982 93	0.000 03
Mg II 2803	2803.5310	1.2589	0.0637	0.982 95	0.000 03
Mg I 2853	2852.9640	0.2608	0.0519	0.982 99	0.000 06

calibrations are based on the latest version of MAPPINGS v5.1 (see Sutherland & Dopita 1993; Dopita et al. 2013) photoionization code. The MAPPINGS photoionization code self-consistently computes the ionization structure of the nebulae, accounting for dust absorption,

radiation pressure, grain charging, and photoelectric heating of small grains (Groves, Dopita & Sutherland 2004).

N18 is based on the latest atomic data for an ensemble of atoms at constant temperature and density. The I06 diagnostic (from Aller 1984) is based on the same model, but uses older atomic data. As a result, both are emission-weighted average temperatures, despite the existence of temperature gradients in real nebulae. The remarkable agreement between T_e derived from I06 and N18 methods is expected because the oxygen atomic data for the relevant lines has not changed substantially.

5.2.2 Ionization parameter

The ionization parameter q is defined as the ratio of incident ionizing photon flux to the hydrogen density at the inner boundary of the ionized shell. It is a measure of the hardness of the ionizing radiation and bolometric luminosity of the ionizing source. We quote q in units of cm s^{-1} throughout this paper. The ionization parameter can also be represented as a dimensionless quantity U, by dividing q by the speed of light.

Table 4. Complete list of all UV and optical diagnostics and the line ratios involved.

Name of diagnostic	Inferred quantity	Line ratio used	Reference
Te_O3a_I06	T_e	[O III] $\lambda\lambda4959,5007$/[O III] $\lambda4363$	Izotov et al. (2006b)
Te_O3a_N18	”	[O III] $\lambda\lambda5007$/[O III] $\lambda4363$	Nicholls et al. (in preparation)
Te_O3b	”	[O III] $\lambda5007$/O III] $\lambda\lambda$ 1660,6	”
Te_O3a_O32 (Direct method)	$12 + \log(\text{O/H})$	Te_O3a_I06 ratios (as above) and [O III] $\lambda\lambda4959,5007$/H β and [O II] $\lambda\lambda3727,9$/H β	Izotov et al. (2006b)
Te_O3b_O32 (Direct method)	”	Te_O3b ratios (as above) and [O III] $\lambda\lambda4959,5007$/H β and [O II] $\lambda\lambda3727,9$/H β	”
KD02N2O2	”	[N II] $\lambda6584$/[O II] $\lambda\lambda3727,3729$	Kewley & Dopita (2002)
PP03N2	”	([O III] $\lambda5007$/H β)/([N II] $\lambda6584$/H α)	Pettini & Pagel (2004)
PPN2	”	[N II] $\lambda6584$/H α	”
S07	”	[Ne III] λ 3869/[O II] $\lambda\lambda3727,3729$	Shi, Zhao & Liang (2007)
BKD18	”	[Ne III] λ 3869/[O II] $\lambda\lambda3727,3729$	Bian, Kewley & Dopita (2018)
D16	”	[N II] $\lambda6584$/[S II] $\lambda\lambda6717,31$ and [N II]/H α	Dopita et al. (2016)
KK04	$12 + \log(\text{O/H})$, $\log(q)$	([O II] $\lambda3727$ + [O III] $\lambda\lambda4959,5007$)/H β and	Kobulnicky & Kewley (2004)
LR14Ne3O2	$\log(q)$	[Ne III] λ 3869/[O II] $\lambda\lambda3727,3729$	Levesque & Richardson (2014)
LR14O3O2	”	[O III] $\lambda\lambda4959,5007$/[O II] $\lambda\lambda3727,9$	”
KD02O32	”	[O III] $\lambda5007$/[O II] $\lambda\lambda3727,9$	Kewley & Dopita (2002)
S18O32	”	[O III]] $\lambda\lambda4959,5007$/[O II] $\lambda\lambda3727,9$	Strom et al. (2018)
S18Ne3O2	”	[Ne III] λ 3869/[O II] $\lambda\lambda3727,9$	”
S18O3Hb	”	[O III] $\lambda5007$/H β	”
K19b Ne3O2	”	[Ne III] λ 3869/[O II] $\lambda\lambda3727,9$	Kewley et al. (2019b)
K19b O3Hb	”	[O III] $\lambda5007$/H β	”
K19b O32a	”	[O III] $\lambda5007$/[O II] $\lambda3727$	”
K19b O32b	”	[O III] $\lambda\lambda1660,6$/[O II] $\lambda2470$a,b	”
K19b C32a	”	[C III] $\lambda\lambda1906,8$/[C II] $\lambda1335$	”
K19b C32b	”	[C III] $\lambda\lambda1906,8,8$/[C II] $\lambda2323-8$	”
Ost_O2	n_e	[O II] $\lambda3729$/[O II] $\lambda3727$	Osterbrock (1989)
S16O2	”	[O II] $\lambda3729$/[O II] $\lambda3727$	Sanders et al. (2016a)
S16S2	”	[S II] $\lambda6731$/[S II] $\lambda6717$	”
K19a O2	n_e, $\log(P/k)$	[O II] $\lambda3729$/[O II] $\lambda3727$	Kewley et al. (2019a)
K19a S2	”	[S II] $\lambda6731$/[S II] $\lambda6717$	”
K19a C3	”	[C III] $\lambda1908$/[C III] $\lambda1906$	”
K19a Si3	”	[Si III] $\lambda1892$/[C III] $\lambda1882$	”

We measure $\log(q)$ using 10 different diagnostics (Table 4): four employ the O_{32} ([O III] $\lambda\lambda4959,5007$/[O II] $\lambda\lambda3727,9$) index from the calibrations of KK04, KD02, Levesque & Richardson (2014, henceforth LR14), Strom et al. (2018, henceforth S18), and new photoionization models of K19b, two are based on the Ne3O2 ([Ne III] $\lambda3869$/[O II] $\lambda3727$) calibrations by LR14, S18, and K19b, and another using the [O III] λ 5007/H β ratio diagnostic from S18 and K19b. Averaging over all the optical SEL diagnostics, we derive a weighted mean $\log(q) = 7.8^{+0.2}_{-0.5}$. We compare the different diagnostics in the top-right panel of Fig. 3 and quote the values in Table 5.

Reddening is a concern for the methods involving the O_{32} ratio, because the [O II] and [O III] wavelengths are widely separated, and hence the dereddened flux obtained for these lines greatly depends on the $E(B - V)$ value and extinction law assumed. As a possible solution, LR14 proposed a new $\log(q)$ diagnostic using the Ne3O2 index, which uses lines with smaller wavelength separation and makes for a more powerful diagnostic in spite of reddening concerns. K19b adds to the LR14 calibrations by using updated photoionization models. We use both methods and compare the results.

The O_{32} and Ne3O2 line ratios are sensitive to metallicity. We use the mean metallicity obtained from all the abundance diagnostics to specify the metallicity branch of the $\log(q)$ calibrations in the LR14 and K19b methods. K19b point out that the Ne3O2 index should only be used when reliable estimates of ISM pressure and metallicity are available. We use the mean ISM pressure derived

using our pressure diagnostics, to define the ISM pressure for use in the K18 methods.

The Ne3O2 diagnostic consistently yields lower (≈ 0.7 dex) $\log(q)$ values than the other diagnostics, for both K19b and LR14 calibrations. This is because the Ne3O2 ratio is extremely sensitive to ISM pressure and metallicity. RCS0327-E yields $\log(P/k) \approx 7.5$ and 8.5 for the low- and high-ionization zones, respectively. The K19b calibrations quoted in this paper correspond to a mean pressure branch of $\log(P/k) = 8.0$. However, the $\log(P/k) = 7.5$ branch of the K19b calibrations yields an ≈ 0.2 dex higher $\log(q)$ and the $\log(P/k) = 8.5$ branch yields ≈ 0.2 dex lower $\log(q)$, compared to the $\log(P/k) = 8.0$ branch. Thus, using $\log(P/k) = 7.5$, brings the Ne3O2 ratio into agreement with the mean $\log(q)$ value derived from other diagnostics. The LR14 diagnostic assumes fixed $n_e = 100$ cm^{-3} ($\log(P/k) \approx 6$), which is not a good approximation for RCS0327-E. S16, on the other hand, include all galaxies, irrespective of their metallicty and pressure, while fitting $\log(q)$ as a function of Ne3O2. This leads to an ~ 0.2 dex intrinsic scatter in the Ne3O2 calibration of S16. Consequently, the $\log(q)$ thus derived, agrees well (within < 0.1 dex) with the mean $\log(q)$, but has a large intrinsic scatter which is not reflected in the quoted uncertainty. The example of RCS0327-E demonstrates the drawbacks of the assumptions in individual emission line diagnostics. It is in such cases that Bayesian inference methods (Section 6) can be more useful, provided the relevant emission lines are available.
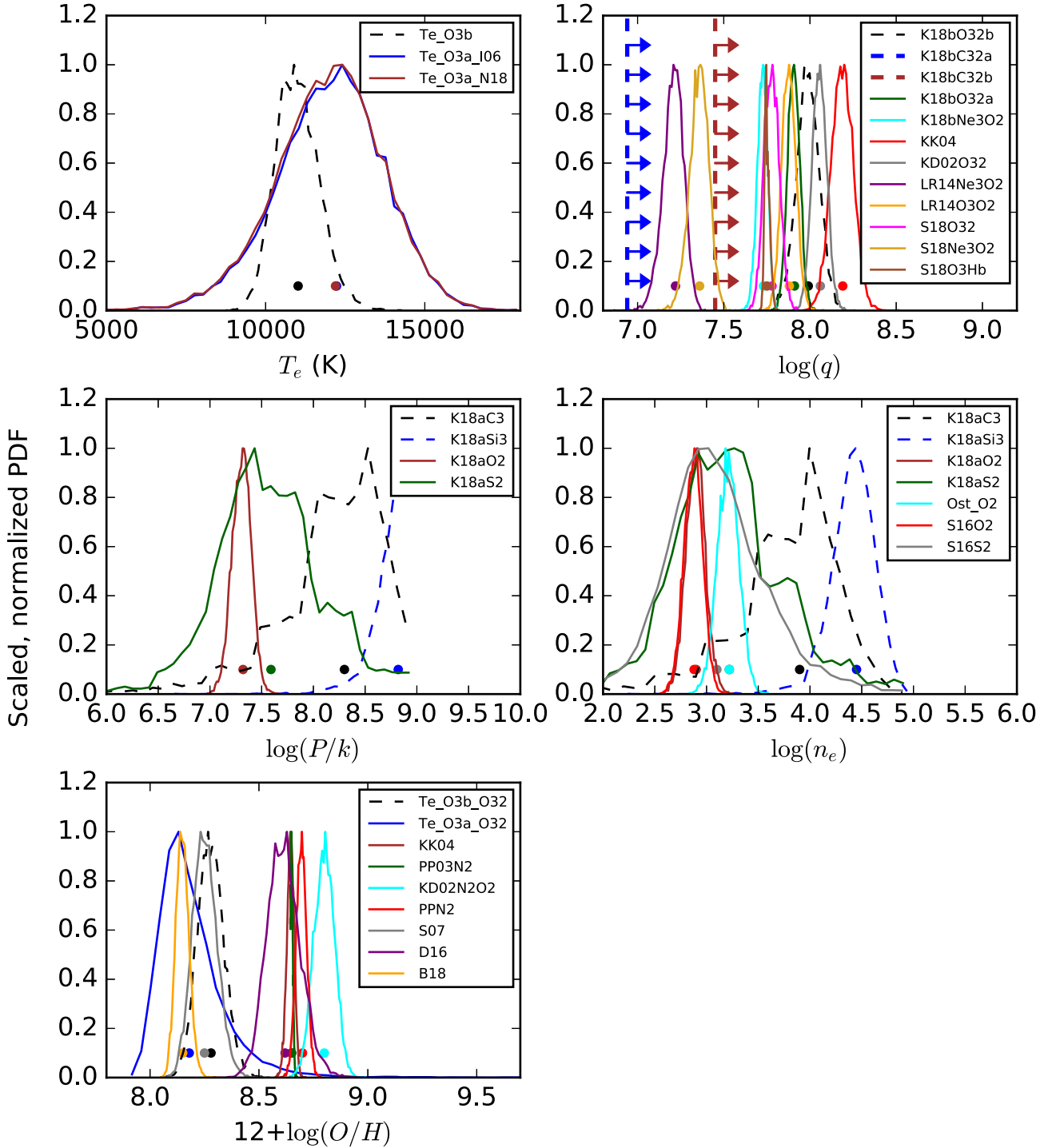
Figure 3. Comparison of individual diagnostics for the physical parameters – electron temperature, ionization parameter, ISM pressure, electron density, and gas phase oxygen abundance. For each panel the curves indicate the normalized, scaled (to unity) probability density function (PDF) of the measured physical quantity generated by performing every diagnostic 10^4 times. For each realization we randomly draw the line fluxes from a Gaussian distribution with mean and width equal to the measured flux and corresponding uncertainty, respectively (see Section 5.1). Different colours denote different diagnostics. The median of each PDF is shown with a filled circle of the corresponding colour. PDFs with dashed lines denote rest-frame UV diagnostics whereas solid lines denote optical diagnostics. The line ratios used for each diagnostic can be looked up in Table 4. For diagnostics involving lines for which we only have upper limits, we do not plot the PDF. Instead, we show the median by thick dashed vertical lines. Whether these are the upper or lower limits of the physical parameter, are denoted by arrows (right arrow: lower limit, left arrow: upper limit). We demonstrate that the UV and optical diagnostics for T_e, log(q), and log(O/H) broadly agree, with some exceptions where the diagnostics either could not be transformed to the common reference frame (for log(O/H)) or used the Ne3O2 index (for log(q)) (detailed in Section 5). For log(P/k) and n_e, however, we find that the UV diagnostics probe different (denser, higher pressure) physical nebular regions than their optical counterparts (detailed in Section 7.5).

Table 5. Inferred physical parameters. The diagnostics (see Table 4 for a list) are discussed in Sections 5.2.5 and 5.3.5. For all further analysis, we consider log(O/H)+12 values in column 3 as the final values, if available. Otherwise we use the values from column 2. We use the $12 + \log(\mathrm{O/H}) = 8.23$ and $\log(P/k) = 8.0$ branch of the K19b diagnostics, for all the K19b diagnostics. K18C32a,b methods have zero uncertainty because they are lower limits on log (q). The values quoted for the IZIP methods correspond to Fig. 4, where a [N II] λ6584/Hα based prior on Z has been used.

Name of diagnostic	Oxygen abundance $12 + \log(\mathrm{O/H})$	$12 + \log(\mathrm{O/H})$ in KK04 frame	Ionization parameter Name of diagnostic	$\log(q(\mathrm{cm\,s^{-1}}))$	ISM pressure Name of diagnostic	$\log(P/k(\mathrm{K\,cm^{-3}}))$	Electron density Name of diagnostic	$\log(n_e(\mathrm{cm^{-3}}))$	Electron temperature Name of diagnostic	T_e ($\times 10^4$ K)
					Optical diagnostics					
Direct (Te-O3a_O32)	$8.19^{+0.16}_{-0.10}$	–	KK04	$8.19^{+0.05}_{-0.05}$	K19a O2	$7.31^{+0.09}_{-0.09}$	Osterbrock O2	$3.21^{+0.10}_{-0.10}$	Te-O3a.I06	$1.22^{+0.16}_{-0.17}$
KK04	$8.65^{+0.02}_{-0.02}$	$8.65^{+0.02}_{-0.02}$	KD02O32	$8.06^{+0.04}_{-0.04}$	K19a S2	$7.59^{+0.51}_{-0.44}$	K19a O2	$2.90^{+0.09}_{-0.09}$	Te-O3a.N18	$1.22^{+0.16}_{-0.17}$
PPN2	$8.32^{+0.02}_{-0.02}$	$8.70^{+0.02}_{-0.02}$	LR14Ne3O2	$7.21^{+0.06}_{-0.06}$	–	–	K19a S2	$3.22^{+0.55}_{-0.46}$	–	–
PPO3N2	$8.21^{+0.01}_{-0.01}$	$8.65^{+0.01}_{-0.01}$	LR14O32	$7.88^{+0.04}_{-0.03}$	–	–	S16O2	$2.88^{+0.09}_{-0.09}$	–	–
KD02N2O2	$8.71^{+0.05}_{-0.06}$	$8.80^{+0.05}_{-0.05}$	K19b O32a	$7.78^{+0.03}_{-0.03}$	–	–	S16S2	$3.1^{+0.5}_{-0.41}$	–	–
S07	$8.26^{+0.25}_{-0.26}$	–	K19b Ne3O2	$7.36^{+0.05}_{-0.06}$	–	–	–	–	–	–
D16	$8.62^{+0.13}_{-0.14}$	–	K19b O3Hb	$7.75^{+0.02}_{-0.01}$	–	–	–	–	–	–
BKD18	$8.15^{+0.03}_{-0.03}$	–	S18O32	$7.91^{+0.04}_{-0.03}$	–	–	–	–	–	–
	–	–	S18Ne3O2	$7.73^{+0.03}_{-0.03}$	–	–	–	–	–	–
	–	–	S18O3Hb	$7.85^{+0.01}_{-0.01}$	–	–	–	–	–	–
					UV diagnostic					
Direct (Te-O3b_O32)	$8.29^{+0.07}_{-0.06}$	–	K18C32a	≥ 6.94	K19a C3	$8.31^{+0.37}_{-0.56}$	K19a C3	$3.91^{+0.36}_{-0.56}$	Te-O3b	$1.10^{+0.07}_{-0.06}$
	–	–	K18C32b	≥ 7.45	K19a Si3	$8.82^{+0.12}_{-0.19}$	K19a Si3	$4.45^{+0.19}_{-0.21}$	–	–
	–	–	K18O32b	$7.99^{+0.07}_{-0.07}$	–	–	–	–	–	–
					IZIP diagnostic					
All lines	$8.56^{+0.07}_{-0.03}$	–	–	–	–	$6.55^{+0.31}_{-0.31}$	–	–	–	–
Only optical lines	$8.53^{+0.03}_{-0.03}$	–	–	–	–	$7.06^{+0.31}_{-0.51}$	–	–	–	–
Only UV lines	$8.04^{+0.13}_{-0.26}$	–	–	–	–	Unconstrained	–	–	–	–
UV + [O II]3727,9	$8.11^{+0.13}_{-0.26}$	–	–	–	–	$7.88^{+0.31}_{-0.20}$	–	–	–	–

5.2.3 Electron density

We compute the electron density n_e in RCS0327-E using the O2 ([O II] λ3729/[O II] λ3727) and S2 ([S II] λ6731/[S II] λ6717) calibrations from Sanders et al. (2016a, hereafter S16) and from the constant density models of K19a. The K19a models cover a range of $\log(n_e/cm^{-3}) = 0$–5, in increments of 0.5 dex. The S16 diagnostics are based on a 5-level atom approximation of the O II and S II ions which yield $\log(n_e) = 2.9^{+0.1}_{-0.1}$ and $3.1^{+0.5}_{-0.4}$ from the O2 and S2 ratios respectively, where n_e is in units of cm^{-3}.

The $\log(n_e)$ we obtain using the K19a O2 and S2 ratios, are in excellent agreement with the corresponding S16 values. K19a provide a 3D (metallicity, ionization parameter, and pressure/density) grid of models with predicted emission line fluxes for every combination of the three parameters. As such, obtaining electron density (or pressure) given a line ratio, requires the metallicity (Z) and ionization parameter (q) as inputs. We use the mean of metallicity and $\log(q)$ values, measured using the different SEL diagnostics, to constrain the Z and $\log(q)$. Thereafter, we interpolate the line ratios as a function of the electron density (or pressure) to obtain our desired physical quantity.

For comparison, we also use the theoretical O2 versus n_e curves from Osterbrock (1989) that are based on single atom models. We infer a weighted mean $\log(n_e) = 3.0^{+0.4}_{-0.2}$ using rest-optical diagnostics. The middle-right panel in Fig. 3 shows our n_e measurements and Table 5 quotes the corresponding values.

The electron density n_e is fundamentally related to the ISM pressure (e.g. see Dopita et al. 2006; Kewley et al. 2019a, for discussion). Assuming a constant electron temperature T_e, the ISM pressure P is related to the total density $n = P/T_e k$ and the total density n is related to the electron density through $n = n_e(1 + (4X + Y)/(2X + 2))$ where X and Y are the mass fractions of hydrogen and helium, respectively. Thus, for a fixed T_e the ISM pressure is directly proportional to n_e. In reality, however, neither the electron temperature nor the density is constant. The ISM is often clumpy and has fluctuations and/or gradients in temperature and density. The constant density models of K19a allow for the temperature structure within the H II region but they do not allow the electron density to vary. Hence, K19a point out that the constant density models are likely to be less realistic than the constant pressure models because typical H II regions have shorter sound crossing time-scale than cooling/heating time-scale, allowing the pressure to equalize throughout the nebula.

5.2.4 ISM pressure

We use the O2 ([O II] λ3729/[O II] λ3727) and S2 ([S II] λ6731/[S II] λ6717) calibrations of K19a to measure the ISM pressure, given in terms of $\log(P/k)$ where k is the Boltzmann constant. We derive a weighted average $\log(P/k) = 7.4^{+0.6}_{-0.2}$ for RCS0327-E from the rest-frame optical diagnostics, where P/k is in units of $K\,cm^{-3}$. The middle-left panel in Fig. 3 shows the PDFs for all diagnostics.

Reddening is not a concern for either of these sets of closely spaced lines. Nevertheless, we performed reddening corrections (as described in Section 5) for consistency. K19a point out that the S2 ratio changes by $\sim$1 dex within a range of $5.5 \leq \log(P/k) \leq 9.0$ and the O2 index drops by $\sim$1 dex within $5.5 \leq \log(P/k) \leq 8.0$, demonstrating that these diagnostics are extremely sensitive to the pressure for this range.

K19a used plane-parallel MAPPINGS v5.1 H II region models at constant pressure, with $\log(P/k)$ ranging from 4.0–9.0 in increments of 0.5. MAPPINGS calculates detailed electron temperature and density structure within the H II region for each of these models at a fixed ISM pressure. K19a point out that the constant pressure models are more realistic than the constant density models used for the electron density calibrations (Section 5.2.3) and recommend using the former. We refer the reader to K19a for a detailed description of the models.

5.2.5 Gas phase oxygen abundance

We measure the gas-phase oxygen abundance from the available set of optical lines in eight different ways (Table 4). We use the combined method of KD02 (section 6; KD02), which, for our abundance regime, uses the [N II] λ6584/[O II] $\lambda\lambda$3727,3729 ratio. We also employ the iterative method of KK04 which uses the R_{23} (([O II] λ3727 + [O III] $\lambda\lambda$4959,5007)/Hβ), and O_{32} indices to solve for both $12 + \log(O/H)$ and $\log(q)$. Both these works stem from MAPPINGS photoionization models of H II regions. We additionally use the N2 ([N II] λ6584/Hα) and O3N2 (([O III] λ5007/Hβ)/([N II] λ6584/Hα)) calibrations from PP04 to compare the abundance values derived using different calibration methods. We also use the empirical Ne3O2 (Ne III] λ 3869/[O II] $\lambda\lambda$3727,9) calibrations from Shi et al. (2007, hereafter S07) and Bian et al. (2018, hereafter BKD18), and the theoretical [N II]/[S II] and [N II]/Hα ratios, following D16. Both the BKD18 and D16 methods are suitable for high redshift ($z \gtrsim 2$) galaxies. In addition to these SEL methods, which depend on photoionization models (with the exception of S07 and BKD18), we also use the direct estimation of the abundance from the electron temperature T_e, following the I06 procedure.

Each method has its own drawbacks. The T_e method, KK04 and KD02 methods are sensitive to reddening corrections because they involve lines with widely spaced wavelengths. The KK04 R_{23} diagnostic is double valued and requires an initial guess of abundance, which we provide by using the [N II] λ6584/Hα ratio. The R_{23} index is also sensitive to ionization parameter $\log(q)$. We use R_{23} in conjunction with the O_{32} index to iteratively solve for both $\log(O/H) + 12$ and $\log(q)$. The S07, BKD18, D16, and both the PP04 diagnostics, do not suffer from reddening issues because they use lines that are closely spaced in wavelength.

In addition to the above shortcomings, all the methods have systematics offsets, relative to one another, on their zero-points (Kewley & Ellison 2008; Bian et al. 2017). This is because of the different photoionization models and samples of H II regions used to derive the diagnostics. The discrepancy between the strong line diagnostics and the T_e method are well known and are mainly attributed to the assumption of a constant temperature in the T_e methods (e.g. Stasińska 2002; López-Sánchez et al. 2012). Additionally, the existence of a temperature gradient within the H II regions may lead the T_e method to systematically underestimate the oxygen abundance because of the assumption of a one or two-zone temperature model (Stasińska 2005). Therefore, it is sensible to compare among these methods, only after we have corrected for the relative offsets.

We correct for this offset following KE08 prescription which was developed using local SDSS galaxies. We convert the $12 + \log(O/H)$ values from the empirical and theoretical calibrations to the reference frame of the KK04 method. The choice for this common reference frame was motivated by the fact that KK04 take into account the dependence of the metallicity sensitive lines on the ionization parameter. However, Kewley & Ellison (2008, hereafter KE08) do not prescribe a conversion scheme from the direct T_e method to the other SEL diagnostics. Therefore, we quote the T_e metallicity as it is, without any conversion. We also transform the R11 abundance

value to the KK04 frame, in order to facilitate comparison between our work and R11. Note that we cannot account for any potential relative offsets in the S07, BKD18, and D16 methods following the KE08 prescription because KE08 predates both.

Table 5 lists the values of $12 + \log(O/H)$ computed using various diagnostics and the bottom-left panel in Fig. 3 shows the corresponding PDFs. Wuyts et al. (2014b) inferred a $12 + \log(O/H) = 8.28 \pm 0.02$ for RCS0327-E, which transforms to $12 + \log(O/H) = 8.65 \pm 0.03$ in the KK04 frame. We plot the Wuyts et al. (2014b) value as a dotted line in Fig. 3 for comparison. Averaging over all diagnostics, we derive a weighted average $12 + \log(O/H) = 8.6^{+0.1}_{-0.4}$ for RCS0327-E in the KK04 frame.

The optical SEL diagnostics yield a weighted mean $12 + \log(O/H) = 8.6^{+0.1}_{-0.4}$. Both the T_e methods and the Ne3O2 methods (S07 and BKD18) result in lower (~ 0.4 dex) abundance. With the exception of BKD18, the other three measurements have large uncertainties associated with them (broad PDFs in Fig. 3). As discussed in Section 5.2.5, the discrepancy between the T_e and strong line methods is well known and can be attributed to the temperature fluctuations and gradients in the H II region, which the T_e methods do not take into account. S07 and BKD18 use the T_e method to calibrate their diagnostic and hence, suffer from the same discrepancy. The higher uncertainties of the T_e and S07 methods are because the [O III] $\lambda4363$ line is often weak or undetected. Moreover, the strong line methods use additional information in terms of $\log(q)$ or a specific branch of metallicity, leading to lower uncertainties.

5.3 Rest-frame UV diagnostics

The rest-frame UV diagnostics use the O III] $\lambda\lambda1660,6$, C III] $\lambda1907$, [C III] $\lambda1909$, and Si II] $\lambda\lambda1883,92$ line fluxes measured from the Magellan/MagE spectra (Table 2). The majority of these diagnostics (refer Table 4) are from recent works of K19a,b and N18, which use the latest, improved version 5.1 of MAPPINGS. The new MAPPINGS v5.1 uses the latest available atomic data from the CHIANTI8 atomic data base (Del Zanna et al. 2015), which is a prime factor that governs the nebular emission line strengths. As described in detail in Section 5.2, the plane parallel isobaric H II region models have been used for both N18 and K18 (except for density diagnostics, where constant density models have been used). Moreover, reddening corrections are not important for the diagnostics involving only rest-frame UV lines, because these pairs of lines have closely spaced wavelengths.

5.3.1 Electron temperature

We derive electron temperature (T_e) using the [O III] $\lambda5007$/O III] $\lambda\lambda1660,6$ ratio from the theoretical calibrations of N18. This method relies on the fact that the $^5S \rightarrow {}^3P$ (λ 5007) and $^1D \rightarrow {}^3P$ ($\lambda\lambda$ 1660,6) transition rate ratio depends only on one physical parameter, the T_e. The other dependencies of the ratio are constants that can be derived from atomic physics. The UV N18 calibrations yield a $T_e = 1.10^{+0.07}_{-0.06} \times 10^4$ K which is ~ 1000 K lower than that derived from the optical T_e diagnostics. The optical and UV T_e measurements agree to within 1σ.

The large wavelength baseline renders the [O III] $\lambda5007$/O III] $\lambda\lambda1660,6$ ratio highly susceptible to uncertainties in reddening corrections. An uncertainty of ±0.07 in $E(B - V)$ leads to $\sim +33$ per cent, -25 per cent uncertainty in this ratio. Moreover, discrepancies in the relative flux calibration from the rest-frame UV to the rest-frame optical spectra can contribute to uncertainties in T_e.

Although we refer to the [O III] $\lambda5007$/O III] $\lambda\lambda1660,6$ method as a UV diagnostic, it still requires [O III] $\lambda5007$. Therefore, no T_e diagnostic used in this paper is completely independent of rest-optical spectra. However, the method involving only the optical lines requires the [O III] $\lambda4363$ line, which is barely detected (SNR = 2.75) in RCS0327-E. Consequently, the [O III] $\lambda5007$/O III] $\lambda\lambda1660,6$ ratio provides a better constraint on T_e. Taking a weighted average of all UV–optical methods, we find a mean $T_e = 1.2^{+0.2}_{-0.1} \times 10^4$ K for RCS0327-E.

5.3.2 Ionization parameter

K19b outline many rest-frame UV emission line ratios that can potentially be used as ionization parameter ($\log(q)$) diagnostics. We choose to use three line ratios: [C III] $\lambda\lambda1907,9$/[C II] $\lambda1335$ (blend of 1334.58, 1335.66, and 1335.71 Å), [C III] $\lambda\lambda1907,9$/[C II] $\lambda2323$-8 (2323.50, 2324.69, 2325.40, 2326.93, and 2328.12 Å) and [O III]] $\lambda\lambda1660,6$/[O II] $\lambda2470$. We derive $\log(q)$ entirely from UV lines, for the first time, by using these three diagnostics. The top-right panel of Fig. 3 shows the PDFs of our $\log(q)$ measurements. The [C II] $\lambda1335$ and [C II] $\lambda2323$ group of lines are not detected in RCS0327-E. We therefore use the 3σ upper limits for the [C II] line fluxes to estimate a lower limit for $\log(q)$, wherever applicable. Lower limits are represented in Fig. 3 as dashed vertical lines with horizontal arrows.

The [C III]/[C II] ratios are very effective measures of the ionization parameter, especially in the low-metallicity regime ($12 + \log(O/H) \leq 8.5$), because they have negligible sensitivity to ISM pressure. Moreover, the [C III] $\lambda\lambda1907,9$/[C II] $\lambda1335$ ratio does not vary with metallicity for low metallicities, making it an ideal $\log(q)$ diagnostic. The [O III] $\lambda\lambda1660,6$/[O II] $\lambda2470$ ratio is analogous to the O_{32} index in optical. K19b advise against the use of the [O III]/[O II] diagnostic in the high pressure ($\log(P/k) \geq 7$) and low-metallicity ($12 + \log(O/H) \leq 8.23$) regime owing to the high sensitivity of these lines (varies > 0.5 dex) to ISM pressure. We derive the ISM pressure of RCS0327-E, and use it to interpolate between the pressure grid, thereby minimizing the sensitivity issue.

The $\log(q)$ estimated from all rest-frame UV and optical diagnostics (except the Ne3O2 ratio) broadly agree within ~ 0.7 dex. K19b O32b is the only UV diagnostic which is not a lower limit, and it yields $\log(q) = 8.0^{+0.1}_{-0.1}$ which agrees with the mean optical result within 1σ uncertainty, as do all the individual K19b diagnostics. The KD02 and KK04 diagnostics were based on an earlier version of MAPPINGS (v3) and as such, yield slightly (~ 0.2 dex) higher $\log(q)$ than the K19b methods, while agreeing to within 1σ with each other. The lower limits on $\log(q)$ obtained from the undetected [C II] emission lines are consistent with the other diagnostics. Although the scatter in ionization parameter is large (~ 0.7 dex), the UV estimates are *not* systematically offset from the optical estimates within the uncertainties, which is encouraging. This clearly demonstrates that it is indeed possible to determine $\log(q)$ using only rest-frame UV spectra, provided at least one of C III] $\lambda\lambda1906,8$/[C II] $\lambda1335$, C III] $\lambda\lambda1906,8$/[C II] $\lambda2325$, or [O III] $\lambda\lambda1660,6$/[O II] $\lambda2470$ ratios is available.

5.3.3 ISM pressure

We determine the ISM pressure ($\log(P/k)$) using the K19a calibrations of rest-frame UV line ratios C III] $\lambda1907$/[C III] $\lambda1909$ (C3) and Si III] $\lambda1883$/Si III] $\lambda1892$ (Si3). These calibrations are derived using the plane-parallel, isobaric model grid from MAPPINGS, as described

in Section 5.2. The middle-left panel in Fig. 3 shows the PDFs of our ISM pressure measurements and the corresponding values are quoted in Table 5. We derive a weighted average $\log{(P/k)} = 8.8^{+0.2}_{-0.6}$ from the UV diagnostics.

In general, the UV diagnostics (dashed lines) yield considerably higher ($\sim$1.4 dex) ISM pressures than the optical diagnostics (solid lines), though there is significant ovelap between the UV and optical PDFs. The discrepancy is the result of the K19a C3 and Si3 diagnostics probing the high pressure ($\log{(P/k)} > 7.5$) regime. We further discuss this difference in Section 7.5.

The Si III and C III ratios approach the high pressure limit at $\sim$1.4 and cease to be sensitive to pressure. Both the pressure diagnostics are sensitive to $\log{(q)}$ and metallicity. The Si III ratio is more sensitive to the ISM pressure, varying by over an order of magnitude in the range $7.5 < \log{(P/k)} < 9.0$, as compared to the C III ratio (which varies by almost an order of magnitude in the same range of $\log{(P/k)}$).

5.3.4 Electron density

Due to the interdependency between the electron density (n_e) and the ISM pressure, the line ratios sensitive to one property are sensitive to the other as well. We derive n_e using the same C3 and Si3 ratios, as in the case of pressure, from the K19a calibrations. However, in this case, the H II region models used assume constant density throughout the nebula, which may not be a valid assumption. We infer a weighted mean $\log{(n_e)} = 4.3^{+0.3}_{-0.6}$ using rest-UV diagnostics.

Note that the K19a C3 and Si3 diagnostics are sensitive only in the high density ($n_e > 1000\ \mathrm{cm^{-3}}$) regime, which holds for RCS0327-E. Both the Si III and C III ratios have almost no dependence on $\log{(q)}$ (figs 1 and 2 in K19a) but are slightly sensitive to the metallicity, which has to be provided in order to obtain n_e.

Similar to the ISM pressure case, we derive consistently higher n_e ($\sim$1.5 dex) with the UV lines than the optical lines, which is reflected as a bimodality in the PDFs in Fig. 3. Again, this discrepancy is the result of different emission line species tracing different physical regions of the nebula, as described in Section 7.5. Thus, it is possible to infer n_e using only the rest-frame UV lines, although the values inferred do not represent the same physical region as the optical diagnostics.

5.3.5 Oxygen abundance

We measure $12 + \log{(O/H)}$ by the direct method following equations (2) and (3) of I06. Here we use the T_e obtained from the [O III] $\lambda5007$/O III] $\lambda\lambda1660,6$ ratio. Because this abundance estimate makes use of the UV lines O III] $\lambda\lambda$ 1660,6 we classify this as a rest-frame UV abundance diagnostic. The UV T_e diagnostic yields $12 + \log{(O/H)} = 8.3 \pm 0.1$, which agrees with the optical T_e abundance within 1σ uncertainty. The bottom-left panel in Fig. 3 compares the abundance diagnostics.

6 JOINT BAYESIAN DIAGNOSTICS

IZI is an IDL-based software developed by Blanc et al. (2015, hereafter B15) that uses Bayesian inference to simultaneously infer metallicity (Z) and ionization parameter ($\log{(q)}$) of the ionized nebular gas. *IZI* requires a set of emission line fluxes observed from the nebulae and a 2D [Z and $\log{(q)}$] grid of models, as its inputs.

We extend the publicly available version of *IZI* to 3D – to enable the metallicity, ionization parameter, and ISM pressure to be

inferred simultaneously. This 3D Bayesian method avoids the need for assumptions about $\log{(P/k)}$ and hence constrains the physical properties in a self-consistent way. The 3D *IZI*, referred to as IZIP (inferring metallicities (Z), ionization, and pressure) henceforth, requires a 3D grid of models (Z, $\log{(q)}$ and $\log{(P/k)}$) as an input to interpolate. We emphasize that IZIP is simply an extension of *IZI* to include an extra dimension, but otherwise preserves the functionality of the original *IZI* algorithm. We use MAPPINGS-V photoionization models to produce a grid of Z, $\log{(q)}$, $\log{(P/k)}$, and emission line fluxes as inputs to IZIP. In the hope that it would benefit the community, we make IZIP publicly available at www.mso.anu.edu.au/acharyya/codes/izip and ask future users to consider this paper as the appropriate reference for IZIP.

The input to the MAPPINGS-V models, which in turn is input to IZIP, accounts for the primary and secondary nucleosynthetic components of the N/O and C/O ratios. The application assumes that the nitrogen and carbon in galaxies have a primary and a secondary origin and that there is no N/O or C/O excess. We are assuming that RCS0327-E lies along the local relation for the above nucleosynthetic origin. Thus, in effect, IZIP accounts for variations in N/O and C/O as a function of metallicity, when used with the MAPPINGS models as the input.

Most individual emission line diagnostics suffer from a major drawback: they are simultaneously sensitive to metallicity, ionization parameter, and pressure. IZIP simultaneously computes the likelihood of each of $12 + \log{(O/H)}$, $\log{(q)}$, and $\log{(P/k)}$ without any assumption about the others. Moreover, IZIP makes use of all the available emission line information simultaneously as opposed to using a specific pair of lines to derive Z and $\log{(q)}$. The Bayesian approach allows us to calculate joint and marginalized posterior PDFs. PDFs allow for multiple peaks and/or asymmetry, which reflect degeneracies in the relation between line fluxes and nebular properties. These degeneracies are harder to deal with while using a specific emission line pair. IZIP also takes into account upper limits for lines that are not formally detected and translates them to a limit on the derived Z, $\log{(q)}$, and $\log{(P/k)}$. This is extremely useful for high-redshift spectroscopic studies for which, often, only upper limits on emission lines are available.

A potential disadvantage of IZIP is that it assumes equal weights on all the available emission lines. In other words, lines that are potentially not sensitive to the concerned nebular property or are also sensitive to other nebular properties are weighted the same as the lines that are only sensitive to the concerned property. Consider, for example, the metallicity. Some metallicity sensitive emission lines are also sensitive to ionization parameter and/or ISM pressure. Individual nebular diagnostics involving these lines would be considered less robust as they may not be ideal probes of metallicity if $\log{(q)}$ and $\log{(P/k)}$ are not accurately known. IZIP, however, is unable to make such informed decisions and would treat these lines with the same weights as other lines that are sensitive to metallicity only (and thus are ideal metallicity indicators). This might lead to poor constraints in the derived metallicity because IZIP includes emission lines that are dominated by other properties (e.g. $\log{(q)}$) which may be dependent on, but not necessarily positively correlated with, metallicity. One way to remedy this would be to provide only those lines to IZIP that are sensitive only to the particular physical parameter. We carry out such tests for different physical quantities and present the results in Appendix A. The issue of using less sensitive emission lines is especially relevant for high-z galaxies because high-z spectra often contain only a few emission lines above a desired SNR threshold, all of which may not necessarily be exclusively sensitive to Z, $\log{(q)}$,

or $\log(P/k)$. Additionally, not all emission lines have a nebular origin. For instance, Prochaska, Kasen & Rubin (2011) suggest that the Mg II and Fe II lines arise due to scattering in the galactic wind. Hence, we remove all the Mg II and Fe II lines, before providing the set of emission lines to IZIP.

Another way to force IZIP to give different weights to different lines is by providing user defined priors to IZIP. For instance, to break the degeneracy of the double valued metallicity branches (e.g. R_{23}), we use a top-hat prior on Z such that $12 + \log(O/H) > 8.52$ if [N II]$\lambda 6584$/H$\alpha > 0.0776$ and vice versa, wherever [N II]/Hα ratio is available. The choice of this prior is motivated by the fact that [N II]/Hα varies monotonically with Z. We chose [N II]/Hα over the [N II]/[O II] ratio because the latter could be affected by relative flux calibration issues as the [N II] and [O II] lines are captured by different NIRSPEC filters. We also investigate the impact of using a flat prior (i.e. no user-defined prior) on the inferred physical quantities in Section 7.4.

To investigate how the ISM properties depend on the amount of spectral information available, we supply IZIP with four different sets of emission lines tailored to mimic observations with different wavelength coverage, as follows:

(i) All the UV and optical emission lines (in Table 6) as input: Using all the nebular spectral information available would help us understand by how much the constraints on the physical properties of RCS0327-E are improved on inclusion of the UV information in addition to the existing optical spectra.

(ii) Only the rest-frame optical emission lines of Table 6: This combination emulates the scenario when the rest-frame UV is not within the observed wavelength coverage and all the information we have is from the rest-frame optical spectra.

(iii) Only the rest-frame UV emission lines of Table 6: We use this combination to study how well the nebular properties can be constrained in a scenario where only the rest-frame UV spectra are available, the redder part of the spectra having been redshifted out of the observed wavelength range.

(iv) The rest-frame UV emission lines along with the [O II] $\lambda\lambda 3727,9$ doublet: The [O II] doublet would be within wavelength coverage until $z \sim 12$ with *JWST*. Hence, combined information from both the [O II] doublet and the UV spectra could be used to infer the physical properties for high-z galaxies.

(v) All the UV and optical emission lines except [Si III] $\lambda\lambda 1882,92$: Excluding the [Si III] doublet allows us to investigate its effect on the inferred nebular properties.

(vi) Only the UV emission lines except [Si III] $\lambda\lambda 1882,92$. This combination of emission lines is one of the many combinations we tested, including or excluding certain emission lines each time. Excluding [Si III] produced a considerable impact, as we discuss in Section 6.1. We discuss all the other additional tests in Appendix A.

IZIP does not account for extinction by dust and requires the user to provide extinction-corrected flux values. We propagate the uncertainties in the reddening value via a Monte Carlo (MC) technique. The MC approach is better than the analytic error propagation because the latter is only applicable up to first-order expansion in Taylor series whereas, given enough iterations, the MC approach better samples the parameter space. We randomly draw from a normal distribution of the measured value of $E(B - V) = 0.4 \pm 0.07$ (W14). After correcting for the reddening using this randomly drawn $E(B - V)$ and Cardelli et al. (1989) reddening law, we supply the dereddened fluxes to IZIP. We repeat this process 100 times, adding and normalizing the resulting PDFs for each

Table 6. List of emission lines provided to IZIP for Bayesian analysis. We provide different combinations of the rest-frame optical and UV emission line fluxes for different cases, as described in Section 6. The third column denotes whether the emission line is undetected and hence upper limits are used by IZIP, or if it is a blended doublet.

Line ID	$\lambda_{\rm rest}$ (Å)	Comments
	Rest-frame UV	
C II 1335a	1334.5770	Upper limit
C II 1335b	1335.6630	Upper limit
C II 1335c	1335.7080	Upper limit
Si II 1533	1533.4312	–
He II 1640	1640.4170	–
O III 1660	1660.8090	–
O III 1666	1666.1500	–
N III 1750	1749.7000	–
[Si III] 1882	1882.7070	–
Si III 1892	1892.0290	–
[C III] 1906	1906.6800	–
C III 1908	1908.7300	–
N II 2140	2139.6800	–
[O III] 2320	2321.6640	–
C II 2323	2324.2140	Upper limit
C II 2325c	2326.1130	–
C II 2325d	2327.6450	–
C II 2328	2328.8380	–
Si II 2335a	2335.1230	Upper limit
Si II 2335b	2335.3210	Upper limit
[O II] 2470	2471.0270	Unresolved doublet
He I 2945	2945.1030	Upper limit
	Rest-frame optical	
[O II] 3727,9	3727.092, 3729.875	Unresolved doublet
[Ne III] 3869	3869.860	–
H ζ	3890.166	–
H δ	3971.198	–
H ϵ	4102.892	–
H γ	4341.692	–
O III 4363	4364.435	–
H β	4862.691	–
[O III] 4959	4959.895	–
[O III] 5007	5008.239	–
H α	6564.632	–
[N II] 6584	6585.273	–
[S II] 6717	6718.294	–
S II 6731	6732.674	–
[Ar III] 7136	7137.770	–

iteration, to give the final marginalized and joint PDFs presented in Section 6.1. The results converge well before the 100 iterations used here.

6.1 Results from Bayesian methods

We describe our results from the Bayesian method, including the cases where different sets of emission lines were provided to IZIP. Figs 4 and 5 show the marginalized PDFs for the different physical parameters and the last section of Table 5 quotes the corresponding peak values. Fig. 5(a) represents the case where all available emission lines were provided to IZIP. For panels Figs 4(c) and 5(b) only rest-frame optical and only rest-frame UV (Table 6) nebular emission lines were used, respectively. The shaded plots denote the 2D PDF (marginalized over the third parameter) and the solid curves denote the 1D PDF for the corresponding physical
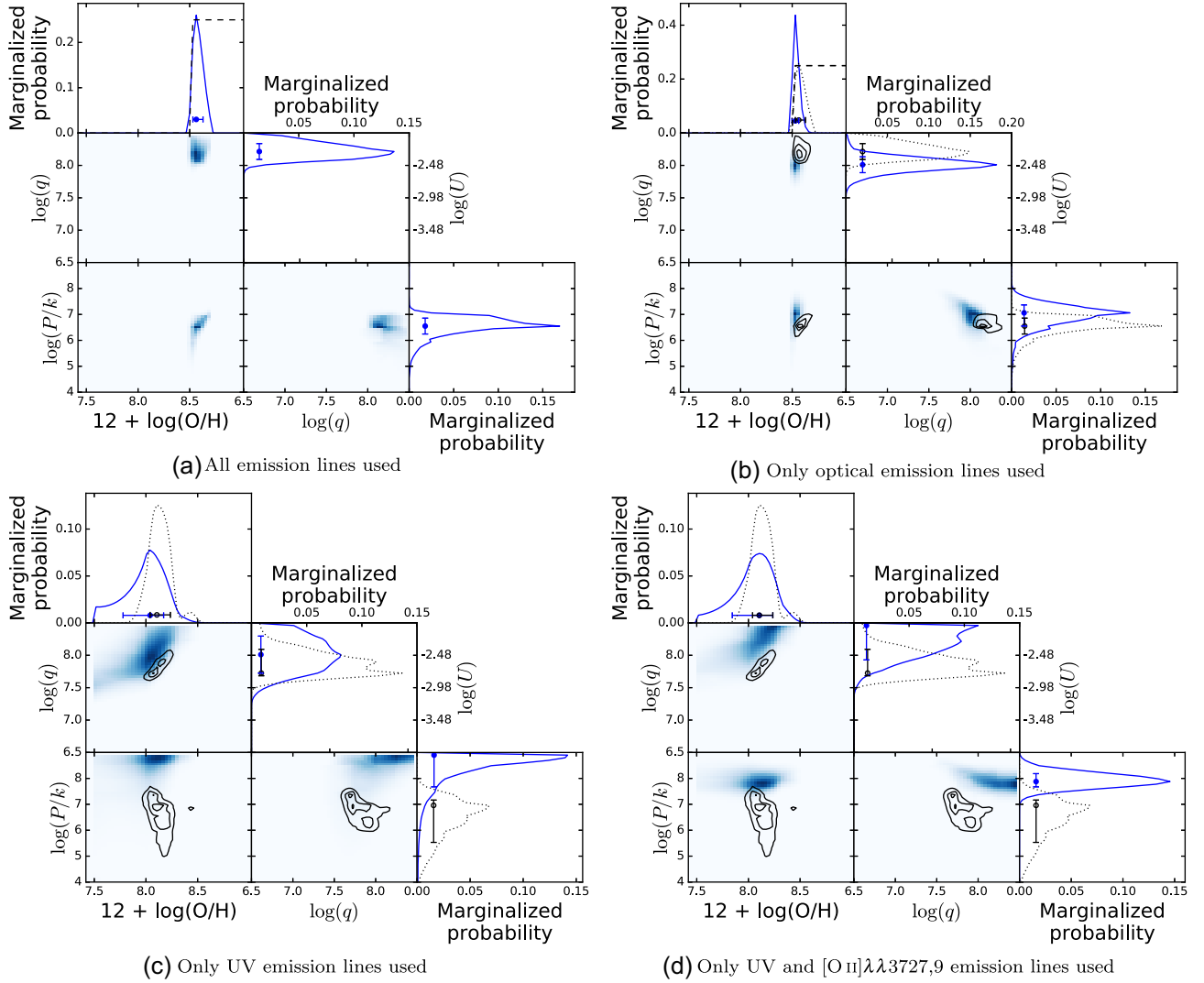
Figure 4. Results from 100 iterations of IZIP (Section 6) with uniform priors on $\log(q)$ and $\log(P/k)$. Wherever both [N II] $\lambda6584$ and Hα are available, we use a top-hat prior on metallicity (black dashed line) such that $12 + \log(O/H) > 8.52$ if [N II] $\lambda6584/H\alpha > 0.0776$ and vice versa. For cases where at least one of the lines is unavailable we use a uniform prior on Z. In each group of plots: the bottom-left plot shows the 2D joint PDF for ISM pressure on the y-axis and metallicity on the x-axis, the middle-left plot shows the 2D joint PDF for ionization parameter (y-axis) and metallicity (x-axis) and bottom-middle plot denotes that for ISM pressure (y-axis) and ionization parameter (x-axis). The remaining plots show the 1D marginalized posterior PDFs for metallicity (top), ionization parameter (middle), and ISM pressure (bottom). The blue circle represents the peak of the marginalized distribution, with error bars being the 16th and 84th percentiles. The top-left group of plots denote results when all rest-frame UV and optical emission lines are used by IZIP. The top-right and bottom-left groups of plots show the results when IZIP works on only the rest-frame optical and only rest-frame UV line measurements, respectively. The bottom-right group of plots corresponds to the scenario where only rest-frame UV and [O II] $\lambda\lambda3727,9$ doublet were provided to IZIP. Fe or Mg emission lines have not been included in the *IZIP* analysis, as discussed in Section 6. The black contours and dotted histograms denote the PDFs (2D and 1D, respectively) of the corresponding fiducial cases i.e. when all the emission lines are used. By definition, the fiducial case for Fig. 4(b) is Fig. 4(a). For Figs 4(c) and (d), we consider the configuration using all the lines but not the [N II]/Hα prior, as the fiducial case (Fig. 5a). We demonstrate that the ISM properties are well constrained on using all the lines or only the rest-frame optical lines. Using UV lines in addition to opitcal lines generally improves the constraints but the UV lines alone find it difficult to constrain metallicity and pressure. Using the [O II] doublet in addition to the UV lines helps constrain the ISM pressure.

parameter. The filled circles at the base of each 1D PDF show the peak value of the PDF, with errorbars being the 16th and 84th perecentiles.

6.1.1 Ionization parameter

The ionization parameter, $\log(q) = 8.21^{+0.12}_{-0.12}$ derived by IZIP using all the emission lines (Fig. 5a), is ~0.4 dex higher than the mean $\log(q) = 7.77^{+0.01}_{-0.01}$ derived using the emission line diagnostics. The

mean $\log(q)$ from the rest-frame optical strong line diagnostics $\log(q) = 7.76^{+0.01}_{-0.01}$ agrees at 1σ level of the peak $\log(q) = 8.01^{+0.12}_{-0.12}$ inferred by IZIP using only the rest-frame optical spectra. The $\log(q) = 8.01^{+0.29}_{-0.29}$ inferred by IZIP while using only the UV spectra agrees with the $\log(q) = 7.99^{+0.07}_{-0.07}$ derived using the rest-frame UV diagnostic of K18, within 1σ uncertainties. This agreement demonstrates that, at least for the test-case of RCS0327-E, the Bayesian *approach* can be used to reliably determine the ionization parameter when only the UV lines are available.
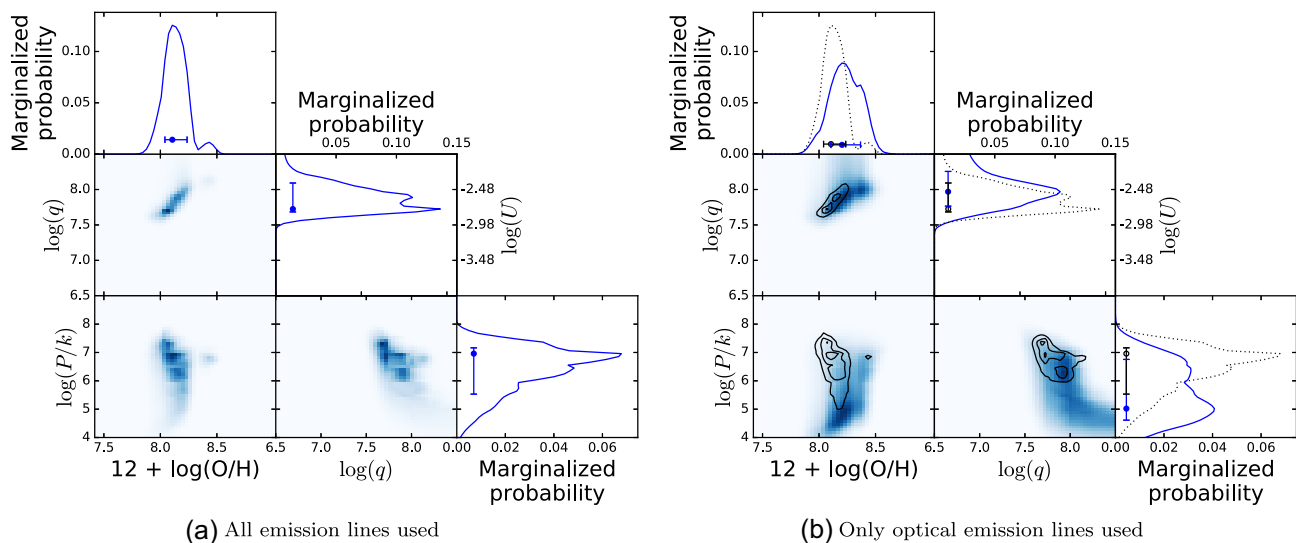
Figure 5. Same as in Fig. 4 but here we use a flat prior on Z even if we include the rest-frame optical emission lines. Fig. 5(a) is shown in Fig. 5(b) with black contours and dotted histograms for visual aid. On using only the optical lines, we infer a lower ($\sim$2 dex), poorly constrained $\log(P/k)$ (right) with a flat prior on Z as compared to using a top-hat prior on Z (Fig. 4b).

6.1.2 ISM pressure

IZIP yields a low $\log(P/k) \sim 7$ (Fig. 4b) when only the optical emission lines are provided. However, using only the UV emission lines results in the $\log(P/k)$ PDF saturating at the edge of the model parameter space (Fig. 4c). Hence, UV lines alone fail to constrain $\log(P/k)$ in the case of RCS0327-E. However, the inclusion of the [O II] $\lambda\lambda3727,9$ doublet with the UV lines (Fig. 4d), constrains the ISM pressure fairly well ($\sigma < 0.4$) at a value $\log(P/k) = \sim 7$ in spite of the inclusion of the high-ionization UV species. This is because the [O II] $\lambda\lambda3727,9$ doublet has much higher SNR than the UV lines and hence gets higher weight during the Bayesian analysis. In contrast, when only the rest-optical lines are used, models predict that the [O II] lines have comparable strength as the [S II] $\lambda\lambda6717,31$ doublet in the high-metallicity regime (such as in RCS0327-E) and hence it is not obvious that [O II] would dominate the Bayesian inference. Moreover, on using the [O II] lines along with the UV lines (Fig. 4d), the PDF is shifted down by $\sim$1.6 dex, implying that the [O II] lines probe a lower ISM pressure than the higher ionized UV species (see Section 7.5). Therefore, the inclusion of [O II] helps to constrain the pressure but also biases $\log(P/k)$ towards lower values than probed by the UV lines.

6.1.3 Oxygen abundance

IZIP infers $12 + \log(O/H) = 8.56^{+0.07}_{-0.03}$ when the full suite of UV and optical spectra is used (top panel, Fig. 4a), which agrees within 1σ of the mean abundance of all the individual diagnostics. The oxygen abundance is poorly constrained by IZIP when only the rest-frame UV spectra are used, suggesting that it is difficult to constrain the abundance using only UV emission lines. The uncertainties in the extreme ultraviolet (EUV) radiation field that is used to produce the H II region models are a potential cause for this difficulty. Providing IZIP with only the UV lines and the Balmer lines does not help improve constraints on $\log(O/H)$ (see Appendix A). Our work implies that rest-frame optical emission lines are necessary to determine the metallicity. It is difficult to obtain reliable metallicity estimates if only rest-frame UV spectra are present. However, we will further investigate the UV sensitivity to metallicity in our future

papers (Acharyya et al. in preparation; Kewley et al. in preparation; Byler et al. in preparation).

7 DISCUSSION

In this section we compare our results based on the availability of different parts of the spectra – UV, optical, UV–optical – in regards to the Bayesian approach. We also discuss our results in the context of previous studies, the implications of our work on upcoming telescopes, and potential caveats.

7.1 Comparison between UV, optical, or UV–optical Bayesian results

7.1.1 Ionization parameter

Ionization parameter values are well constrained when only optical emission lines are provided to IZIP, along with an user defined prior on Z based on [N II] $\lambda6584/H\alpha$ (Fig. 4b). However, inferring $\log(q)$ from only the optical lines or only the UV lines, in absence of a prior, shows a broad tail (small likelihood) of high $\log(q)$ values and hence put a poorer constraint on $\log(q)$. The bias towards high $\log(q)$ is more pronounced when the [O II] $\lambda3727$ doublet is included in addition to the UV lines, leading to an unconstrained PDF. The $\sim$0.2 dex higher $\log(q)$ inferred by using all the emission lines, compared to when only the UV or optical lines are used, is not concerning given that the values still agree within 1σ. The blue and black dotted histograms for $\log(q)$ in Figs 4(b), (c), and 5(b) have considerable overlap to demonstrate the agreement within the uncertainties. We conclude that adding the rest-frame UV information to the existing optical spectra, puts a better ($\sigma \sim 0.2$) constraint on $\log(q)$ overall, than when only the optical spectra are used. The UV lines by themselves barely constrain $\log(q)$, albeit with a larger uncertainty than when all lines are used.

7.1.2 ISM pressure

In the event of only the UV lines being available, the Bayesian approach would give an ISM pressure value of $\log(P/k) = 8.90^{+0.10}_{-1.22}$

whereas, inclusion of the [O II] $\lambda\lambda3727{,}9$ lines would yield a lower $\log(P/k) = 7.88^{+0.31}_{-0.20}$). Both these values agree (within 1σ uncertainties) with $\log(P/k) = 8.8^{+0.2}_{-0.6}$ and $\log(P/k) = 7.4^{+0.6}_{-0.2}$ derived from the individual UV and optical emission line diagnostics, respectively. This demonstrates that with a rest-frame UV coverage up to the [O II] $\lambda\lambda3727{,}9$ lines, it is possible to effectively probe the different physical regions in the nebula using the Bayesian approach. Suitably designed future surveys with the *JWST* should take advantage of this fact.

7.1.3 Oxygen abundance

When only optical lines are used, IZIP shows a double-peaked PDF (Fig. 5b), with the stronger peak being at $12 + \log(\mathrm{O/H}) = 8.20^{+0.16}_{-0.10}$, reflecting the fact that the optical collisionally excited emission lines are doubled valued with metallicity. For the case where only UV lines are used (Figs 4c and d), the abundance PDF has a broad low-metallicity tail, with a peak at $12 + \log(\mathrm{O/H}) = 8.04^{+0.13}_{-0.26}$. Providing IZIP with the [O II] $\lambda3727$ doublet along with the UV lines (Fig. 4d) helps constrain the oxygen abundance to a slightly ($\sim$0.07 dex) higher value $12 + \log(\mathrm{O/H}) = 8.11^{+0.13}_{-0.26}$ but does not lead to better (narrower) constraints. The broader $12 + \log(\mathrm{O/H})$ PDFs when only UV lines are used, imply that it is difficult to infer the oxygen abundance with only the rest-frame UV lines using a Bayesian approach.

7.2 Comparison with other work

In this section we compare the physical properties of RCS0327-E with those of other galaxies from the literature, over a wide range of redshifts. However, one should bear in mind that RCS0327-E is an $\sim$100 pc region of vigorous star formation whereas most of the literature data correspond to spatially integrated spectra of entire galaxies that include both star-forming regions as well as passively evolving stellar populations. As such, some ISM parameters e.g. $\log(q)$ are expected to be higher in RCS0327-E than the spatially averaged properties of other galaxies.

7.1.2 Electron temperature

van Zee & Haynes (2006) studied a sample of nearby dwarf galaxies and reported the ISM $T_e \sim 1.3 \times 10^4$ K. Jones et al. (2015) obtained $T_e \leq 2 \times 10^4$ K for a sample of 32 $z \sim 0.8$ galaxies. On the other hand, Yuan & Kewley (2009) reported a $T_e = 2.3 \times 10^4$ K for a lensed galaxy at a redshift $z \sim 1.7$. Christensen et al. (2012) estimated 1.3×10^4 K $\gtrsim T_e \gtrsim 2.7 \times 10^4$ K for three lensed galaxies in the redshift range $2 \gtrsim z \gtrsim 3.5$. Further adding to the sample of lensed galaxies, Stark et al. (2013) and James et al. (2014) estimated $T_e \sim 1.5$ and 1.7×10^4 K for two galaxies at $z \sim 1.4$. Steidel et al. (2014) reported a mean T_e of $\sim$1.3 $\times 10^4$ K for 3 KBSS-MOSFIRE galaxies at redshift $\sim$2. Sanders et al. (2016b) estimated an [O III] $T_e = 1.4^{+0.20}_{-0.14} \times 10^4$ K, and Bayliss et al. (2014) derived an upper limit on $T_e \leq 1.4 \times 10^4$ K for two galaxies at $z \sim 3$ and 3.6, respectively. Thus, RCS0327-E has a [O III] T_e ($1.2^{+0.2}_{-0.1} \times 10^4$ K) similar to that of local galaxies, and marginally lower than that of $z \sim 2$–3 galaxies.

7.2.2 Ionization parameter

We derive a weighted mean $\log(q) = 7.77 \pm 0.01$ for RCS0327-E, averaging over all the diagnostics. The mean $\log(q)$ agrees with the study of $z \sim 2$–3 galaxies by Steidel et al. (2014) where they reported $\log(q)$ values between 7.6 and 8.7 using CLOUDY photoionization models. Moreover, Kaasinen et al. (2018) analyse spectra from $\sim$200 000 SDSS galaxies and derive a mean $\log(q) = 7.4$ (using both KK04 and IZI), further supporting the scenario that ionization parameter at high ($z \sim 2$) redshift is higher than that in the local niverse (Steidel et al. 2014; Kewley et al. 2015; Strom et al. 2017).

7.2.3 Electron density

S16 measured a mean $\log(n_e/\mathrm{cm}^{-3}) \approx 2.4$ for 225 star-forming galaxies at $z \sim 2.3$ with median stellar mass of $M_* = 10^{10}\,M_\odot$ and median SFR $= 21.6\,M_\odot\,\mathrm{yr}^{-1}$. In agreement with S16, Strom et al. (2017) reported a mean $\log(n_e/\mathrm{cm}^{-3}) \approx 2.44$ for another high-redshift ($z \simeq 2$–3) sample of $\sim$380 galaxies, whereas Kennicutt (1984) measured electron densities between $2 \leq \log(n_e/\mathrm{cm}^{-3}) \leq 3$ for H II regions in nearby galaxies. The Strom et al. (2017) sample consists of star-forming galaxies with $M_* = 10^9$–$10^{11.5}\,M_\odot$ and SFR $= 3$–$1000\,M_\odot\,\mathrm{yr}^{-1}$, which encompasses the properties of RCS0327 ($M_* = 10^{10}\,M_\odot$ and SFR $= 60\,M_\odot\,\mathrm{yr}^{-1}$). The local galaxies of the Kennicutt (1984) sample, however, are quiescent galaxies spanning $M_* = 10^8$–$10^{11}\,M_\odot$ and SFR $\leq 1\,M_\odot\,\mathrm{yr}^{-1}$. All of these studies used rest-frame optical spectra to determine n_e. RCS0327-E has a slightly higher electron density ($\log(n_e) \simeq 3.04$) than both the local and $z \simeq 2$–3 galaxies. Kaasinen et al. (2017) study a sample of $z \sim 1.5$ galaxies with median $M_* = 10^{7.5}\,M_\odot$ and SFR $= 15\,M_\odot\,\mathrm{yr}^{-1}$ and report $\log(n_e) \simeq 2.05$. Their M_*- and SFR-matched local analogues yield $\log(n_e) \simeq 1.99$. RCS0327 being more massive and more rapidly star forming than the $z \sim 1.5$ sample, has a higher ($\sim$1 dex) electron density.

7.2.4 Oxygen abundance

Fig. 6 shows the evolution of oxygen abundance as a function of redshift and where, in that evolutionary track, RCS0327 lies with its stellar mass content of $<10^{10}\,M_\odot$ (Wuyts et al. 2014a). We adopt the mean abundance values in table 2 of Yuan et al. (2013) to compare with our work. The $12 + \log(\mathrm{O/H}) = 8.32 \pm 0.02$ for RCS0327-E derived from the [N II] $\lambda6584$/Hα diagnostic of PP04 (PPN2) is shown in Fig. 6 (red star) in order to be consistent with Yuan et al. (2013). The abundance of RCS0327-E ($z \sim 1.7$), based on PPN2, is also comparable to those of other high-redshift studies like Jones et al. (2010, $z \sim 2.0$), Shapley et al. (2004, $z \sim 2.0$), and Steidel et al. (2014, $z \sim 2.3$) that report $12 + \log(\mathrm{O/H}) \simeq 8.4$–8.5 using PPN2. The metallicity of RCS0327-E is $\sim$0.2 dex lower than that of the local galaxies of KINGFISH survey, which are reported to have $12 + \log(\mathrm{O/H}) \sim 8.5$ (converted to PPN2 frame using KE08) by Kennicutt et al. (2011). Using Bayesian methods, Kaasinen et al. (2018) find $12 + \log(\mathrm{O/H}) = 8.7$ for local galaxies and $12 + \log(\mathrm{O/H}) = 8.0$ for redshift $z \sim 1.5$ galaxies, in the mass bin $9 < \log(M_*/M_\odot) < 10$. Bayesian (using IZIP) abundance estimates for RCS0327-E are $\sim$0.2 dex lower and $\sim$0.5 dex higher than the low- and high-redshift measurements of Kaasinen et al., respectively. Thus, RCS0327-E is consistent with the trend of decreasing oxygen abundance with redshift.

7.3 Implications for *JWST*

In this work, we have used the O III] $\lambda\lambda1660{,}6$ lines in the UV (along with [O III] $\lambda5007$) to directly determine the oxygen abundance from T_e. We have also inferred the abundance using a Bayesian approach
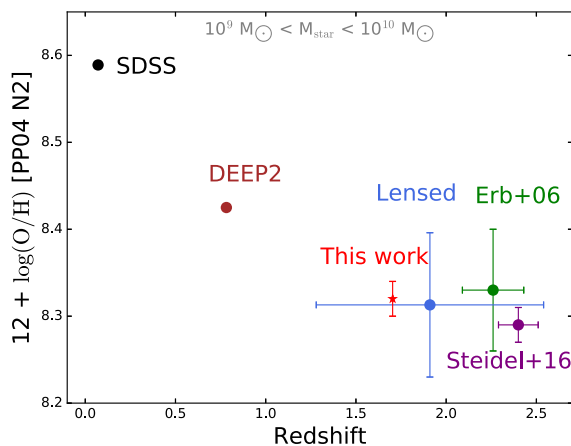
Figure 6. Redshift evolution of oxygen abundance in the stellar mass bin $10^9 \, \mathrm{M}_\odot < M_* < 10^{10} \, \mathrm{M}_\odot$, based on Yuan et al. (2013). Yuan et al. (2013) obtained the SDSS (black) and DEEP2 (brown) data from Zahid, Kewley & Bresolin (2011) and the green point from the UV-selected Erb et al. (2006) galaxies. The 'Lensed' (blue) data denote the mean abundance for the lensed sample in Yuan et al. (2013), which also includes measurements from Yuan et al. (2011), Wuyts et al. (2012b), and Richard et al. (2011). The $12 + \log(O/H)$ we derived using the [N II] $\lambda 6584/\mathrm{H}\alpha$ diagnostic of PP04 (PPN2) is shown as a star, while all the other mean abundance values have been taken from table 2 of Yuan et al. (2013) and are denoted by circles. We show only the PPN2 diagnostic in this plot in order to be consistent with Yuan et al. (2013). The uncertainties quoted for the SDSS and DEEP2 samples by Yuan et al. (2013) is the 1σ standard deviation of the mean from bootstrapping. Uncertainties thus derived are too small to be visible on this scale, because the surveys comprise of a large number of galaxies. In addition to table 2 of Yuan et al. (2013), we also include $12 + \log(O/H)$ measurement of the composite spectrum from Steidel et al. (2016) as a purple circle.

by providing the UV line and [O III] $\lambda 5007$ to IZIP (see Appendix A). From both these tests we conclude that it is difficult to reliably estimate metallicity with only the rest-frame UV lines – the [O III] $\lambda 5007$ line is required to break the degeneracy. *JWST*/NIRSpec will be able to simultaneously capture the [O III] $\lambda 5007$ line and the [O III] $\lambda\lambda 1660,6$ doublet within redshift $3.5 \lesssim z \lesssim 9$, thereby making it possible to obtain reliable estimates of oxygen abundance at such high redshifts. Currently, rest-frame UV nebular emission line diagnostics for oxygen abundance are scarce. However, K19b and Byler et al. (in preparation) investigate the diagnostic power of the UV lines, in detail.

We demonstrate that $\log(q)$ can be determined using only rest-frame UV spectra, provided at least one of [C III] $\lambda\lambda 1906,8$/[C II] $\lambda 1335$, [C III] $\lambda\lambda 1906,8$/[C II] $\lambda 2325$, or [O III] $\lambda\lambda 1660,6$/[O II] $\lambda 2470$ ratios is available (Section 5.3.2). These ratios will be within the wavelength coverage of *JWST*/NIRSpec for redshifts above $z \sim 3.5$, 1.6, and 2.6, respectively. However, the [C II] $\lambda 1335$ group is very weak ($\sim 10^{-3}$–$10^{-4} \times \mathrm{H}\beta$ flux for $\log(q) = 8.0$ and $Z = 0.4 \, \mathrm{Z}_\odot$). The unresolved [C II] $\lambda 2325$ group of lines is very closely spaced in wavelength, thereby making it difficult to estimate the fluxes for moderate resolution spectra. Large uncertainties stemming from line blending could potentially be translated into uncertainties in $\log(q)$.

7.4 IZIP with and without priors

A point to note about the Bayesian inference method is that collisionally excited emission lines are double valued with metallicity. IZIP, by default, is unable to make an informed choice between

the two branches based on specific emission line ratios, and yields bimodal PDFs in many such cases. For instance, one could not use the [N II] $\lambda 6584/\mathrm{H}\alpha$ ratio to break the degeneracy while using the R_{23} metallicity indicator. Instead, IZIP would use the R_{23} line flux information and weigh them same as all the other lines, thus leading to a double-peaked metallicity PDF. This is not wrong from a Bayesian perspective, because the models indeed predict two probable values of $\log(O/H)$ given the emission line ratios. However, the observed H II region can only have one or the other abundance; this is where an observer would use other emission line information to decide between the two branches. To facilitate this, IZIP takes into account user defined priors on the physical parameters while computing the posterior distribution. Providing user-defined priors to IZIP based on certain line ratios can help break the degeneracy.

We impose a top-hat prior on the [N II] $\lambda 6584/\mathrm{H}\alpha$ ratio, where available (discussed in Section 6), to help select the relevant metallicity branch. In the absence of a prior, we infer $12 + \log(O/H) = 8.53^{+0.1}_{-0.07}$ when the full suite of UV and optical spectra is used (Fig. 5a); and $12 + \log(O/H) = 8.20^{+0.16}_{-0.1}$ when only the rest-frame optical lines are used (Fig. 5b). This discrepancy in $\log(O/H)$ based on whether UV lines are included could be potentially due to inconsistencies in photoionzation models, as discussed in Section 7.6. On using the prior on [N II]/$\mathrm{H}\alpha$, the oxygen abundance is well constrained to a peak value of $12 + \log(O/H) = 8.56^{+0.06}_{-0.03}$ (Fig. 4a) and $12 + \log(O/H) = 8.53^{+0.03}_{-0.03}$ (Fig. 4b) by using UV–optical and only optical lines, respectively. In Fig. 4(b), the top-hat prior used to derive the posterior probability is shown by a black dashed line in the 1D PDF of the metallicity (top) panel. Using the [N II]/$\mathrm{H}\alpha$ prior leads to narrow constraints, as expected, and closer agreement between the abundances measured with different set of emission lines. Comparing Figs 4(a) with 5(a) and Figs 4(b) with 5(b) reveals that usage of a prior on abundance, also has considerable impact on $\log(q)$ and $\log(P/k)$. The high-$\log(q)$ and low-$\log(P/k)$ solution is eliminated on using the prior, leading to much tighter constraints on both these physical properties. We therefore recommend employing priors where possible (e.g. [N II]/$\mathrm{H}\alpha$ available), to break the degeneracy while using IZIP.

7.5 ISM pressure – UV versus optical

ISM pressures measured using the new UV diagnostics are ~ 1.5 dex higher than those determined using optical line ratios. This discrepancy can be attributed to the fact that the different emission lines originate from different regions of the ionized ISM. As K19a point out, the regions closer to the ionizing source receive a greater proportion of the UV photon flux resulting in a greater fraction of higher ionization species. Consequently, the higher ionization emission lines in the rest-frame UV probe the inner, high-pressure region of the nebula, whereas the lower ionization lines in the optical probe the outer, lower pressure zone. This is due to the different sensitivity of various emission species to different density regimes depending on critical density. It is therefore unsurprising that we would derive a higher pressure and higher density with the UV diagnostics.

Fig. 7 shows the emissivity of various line species as a function of the depth into the nebula. Higher ionization species (rest-frame UV diagnostics) used in this work – [C III] and [Si III] are produced throughout the H II region, and concentrated in the inner regions ($\lesssim 70$ per cent of nebular shell radius). In contrast, the lower ionization species (rest-frame optical diagnostics) used in this work – [O II] and [S II] are primarily produced in the outer parts
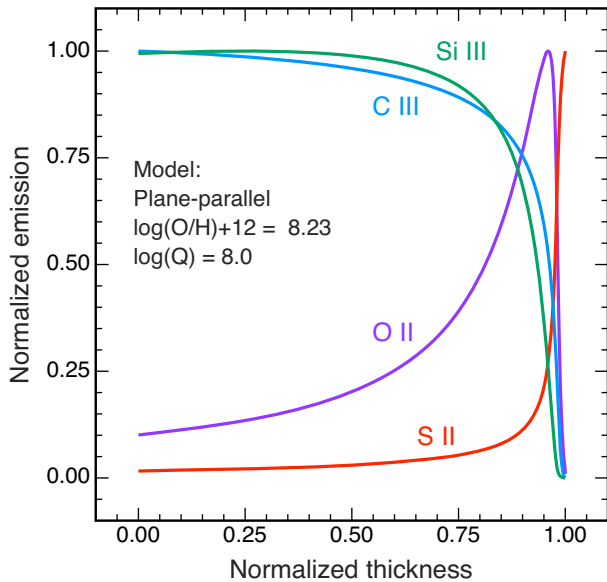
Figure 7. Normalized strength of different emission line species as a function of normalized shell thickness. The high ionization species C III and Si III originate from inner, denser zones of the nebula whereas the lower ionization O II and S II ions trace the less dense peripheral part of the ionized nebular shell. The curves correspond to a MAPPINGS photoionization H II region model, assuming plane-parallel geometry, for $12 + \log(O/H) = 8.23$ and $\log(q) = 8.0$.

of the nebula, specifically, from ∼80 per cent and ∼100 per cent of the nebular shell radius. We might expect that the [C III] and [Si III] species represent the average physical conditions within ≲70 per cent of nebular shell radius, whereas the [O II] and [S II] species probe the H II region at 80 per cent radius and extreme outskirts, respectively.

Our work demonstrates that, given only the rest-frame UV spectra, it is possible to derive $\log(P/k)$ (or n_e) using the SEL diagnostics. Whether the Bayesian methods can reliably constrain $\log(P/k)$ using only the UV lines remain unclear. However, one has to bear in mind that the $\log(P/k)$ (or n_e) derived from the SEL diagnostics would be representative of the inner regions of the nebula and consequently would be biased towards higher values. There is no clear choice for a 'better' diagnostic between the different UV and optical diagnostics. It is simply a case of different emission line species probing different physical regions in the nebulae.

Rest-frame optical spectra, when available, probe the outskirts of the nebula. Additionally including rest-frame UV spectra probe the inner physical regions of the nebula as well. K19a suggest using the Si IIIλ33 μm and Cl IIIλ5518 Å lines as diagnostics that are more representative of the entire nebula because these emissions originate fairly uniformly throughout the nebula. However, we do not detect either of these emission lines in RCS0327-E.

The measured electron densities are not representative of the entire nebula either. Different emission lines have different critical densities, making them sensitive to different density regimes. K19a point out that the density structure of an H II region can be quite complex. Moreover, clumpy star formation knots have been observed in RCS0327. As such, it is more sensible to measure the ISM pressure in this case than measuring a constant density which may not be representative of the entire ionized ISM.

The above discussion naturally raises a general (not specific to ISM pressure) concern regarding the combined usage of the emission lines originating in inner nebular regions with those emitted from the outer regions. While this is a valid concern, the extent to which such combined usage would make a difference depends on the particular emission line ratio and the ISM property involved. In case of $\log(P/k)$ and n_e, all the lines involved in a particular diagnostic are of the same ionization species which originate at similar physical regions, but different diagnostics have lines originating from different regions, indicating that each diagnostic clearly probes a different nebular region. As such, it is not sensible to combine the two groups – UV and optical diagnostics – for pressure and density measurements and should be considered as probes of distinctly different nebular regions. For abundance and ionization parameter, however, some diagnostics involve emission lines of different ionization species e.g. the R23, O_{32} and Ne3O2 ratios (see Table 4). The [O III] lines originate throughout the nebula, implying that the R_{23} and O_{32} diagnostics are representative of the entire gas cloud. Thus, it is sensible to compare diagnostics involving [O III] with other diagnostics for $12 + \log(O/H)$ or $\log(q)$. It is difficult to compare Ne3O2 index with other diagnostics as the former yields systematically different values of $12 + \log(O/H)$ or $\log(q)$, due to reasons discussed in Section 5. Moreover, these diagnostics are based on models for a single H II region. whereas in reality, a star-forming knot would comprise of several such H II regions. Thus, we probe the emission-weighted average properties of an ensemble of H II regions. We conclude that, it is possible to combine rest-frame UV and optical diagnostics; modulo the fact that they probe different physical regions in the case of pressure and density. We refer the reader to K19b for a review of ionization parameter and metallicity diagnostics.

7.6 Caveats

One potential reason for the discrepancy between the ISM pressure (∼1.5 dex) and oxygen abundance (∼0.5 dex) derived from UV and optical emission lines, is inconsistencies in the inputs to the H II model grid. The currently available stellar atmosphere libraries and stellar evolutionary tracks are based on different abundance standards and do not agree. The O-star models are only sparsely represented in the available model sets. Moreover, the stellar population synthesis (SPS) model Starburst99 (Leitherer et al. 1999) linearly interpolates between these sparsely sampled libraries.

A second, but less concerning, source of uncertainty comes from the scatter in the available atomic data, which leads to a variation in the ionizing energies of crucial nebular emission lines (up to a factor of 2). Thus, there is an intrinsic uncertainty in the input stellar spectra. For instance, the stellar spectra obtained from Starburst99 in different spectral resolution modes do not agree in the rest-frame UV regime. Nevertheless, in the absence of more extensive stellar model sets, the Starburst99 spectra are used by the photoniozation code MAPPINGS v5.1 (Dopita et al. 2013) as the driving source of the radiation field leading to all the high ionization emission lines. The inherent discrepancy in Starburst99 translates to uncertainties in output UV and optical emission line fluxes in the H II region model grids of MAPPINGS. The MAPPINGS model grids, in turn, have been used to calibrate the K19a diagnostics. Thus, there are inherent discrepancies in the rest-frame UV diagnostics. Moreover, our Bayesian analysis is also based on the MAPPINGS model grids. This could potentially lead to discrepancies in the metallicity determined using only UV or only optical emission lines.

Different SPS models incorporating different physics could potentially have an impact on the ionizing stellar spectra used as an input to the photoionization models, but such a comparative study is

beyond the scope of this paper. However, D'Agostino et al. (2019) have recently compared different SPS models and concluded that for most cases the emission line *ratios* do not change considerably. The ionizing spectra were found to be somewhat sensitive to the cluster age and SPS codes, extremely sensitive (∼8 orders of magnitude) to stellar evolutionary tracks, with very little (≲2 per cent) dependence on the stellar atmospheres and the inclusion of binaries. D'Agostino et al. (2019) however, have not investigated the impact of different functional forms for the initial mass function (IMF) on the spectra.

Work is currently in progress to combine stellar atmosphere models and evolutionary tracks with improved, stochastic SPS codes. Once complete, we will have state-of-the-art diagnostics with self-consistent inputs and will be able to determine how much of the observed discrepancy in physical parameters stems from the observed target itself. Given all uncertainties in the models, we can constrain the physical properties remarkably well within the observed level of agreement. Moreover, the caveats discussed in this section are likely to have a smaller effect on the $\log(P/k)$ measurements than the fact that UV and optical lines probe different physical nebular regions.

8 SUMMARY AND CONCLUSIONS

We measure equivalent widths and fluxes of the emission lines in the rest-frame UV and optical spectra of RCS0327-E. By applying the full suite of new and existing UV and optical SEL diagnostics on the dereddened fluxes, we determine the ISM properties of RCS0327-E. We show that it is possible to infer some of the ISM properties – ionization parameter, electron density, and ISM pressure in the inner nebular region – with only the rest-frame UV emission lines. The rest-frame optical spectra better constrain the abundance and probe the pressure and density at the outer nebular regions.

We develop a new extension of IZI, called IZIP, which uses Bayesian inference method to simultaneously infer $12 + \log(\text{O/H})$, $\log(q)$, and $\log(P/k)$ values. Given a theoretical model grid of emission line fluxes and a set of observed emission lines, IZIP constrains the three physical parameters simultaneously. We run IZIP with four different sets of emission lines – all available emission lines, only the rest-frame UV lines, only the optical lines and UV + [O II] λλ3727,9 lines – to mimic observations with different rest-frame wavelength coverage.

By comparing the individual emission line diagnostics and the results from the four different configurations of IZIP, we draw the following conclusions:

(i) The rest-frame UV emission lines infer ∼1.5 dex higher ISM pressures than the optical emission lines, because they probe different physical regions. The latter probe the outskirts of the nebula whereas the higher ionization UV species probe the inner, denser regions. Because it is directly related to ISM pressure, the electron density also exhibits the same behaviour.

(ii) The rest-frame UV emission lines used in this work (see Table 6) are insufficient to accurately constrain the oxygen abundance for RCS0327-E. The [O III] λ5007 emission line, used along with O III λλ 1660,6, [O II] λλ3727,9 and H β, helps constrain the oxygen abundance through the direct (T_e) method, and is within range of *JWST*/NIRSpec wavelength coverage for redshifts $z \lesssim 9$.

(iii) If only rest-frame UV spectra are available, it is possible to derive the ionization parameter $\log(q)$ as long as at least one of the ([C III] λ1906 + λ1908)/[C II] λ1335, ([C III] λ1906 + λ1908)/[C II] λ2325, or ([O III] λ1660 + λ1666)/[O II] λ2470 ratios are available.

JWST/NIRSpec will be able to capture these ratios in the redshift ranges $3.5 \lesssim z \lesssim 27$, $2.1 \lesssim z \lesssim 22$, and $2.6 \lesssim z \lesssim 20$, respectively.

(iv) Joint Bayesian analysis is useful to determine $\log(q)$ and $\log(P/k)$ when the rest-frame optical lines are available and yield results comparable to SEL diagnostics. Bayesian techniques have the capability to explore non-trivial topology in the PDFs of the inferred parameters e.g. multiple peaks and asymmetry. However, when only the UV lines listed in Table 6 are available, it is difficult to constrain the oxygen abundance using Bayesian methods and currently available photoionization grids. Inclusion of [O II] λλ3727,9 with the UV lines does not make a noticeable difference either. This is a potential problem for *JWST* at very high redshifts if the [O III] λ5007 line is not available to break the degeneracy.

(v) Given rest-frame UV coverage and the optical [O II] λλ3727,9 doublet, it is possible to effectively probe the ISM pressure in different physical regions in the nebula using the Bayesian approach. Future surveys with the *JWST* will be designed to take advantage of this fact.

In summary, we have demonstrated the power of rest-frame UV emission line diagnostics used in conjunction with rest-frame optical diagnostics, for inferring the ionized gas properties of moderate to high-redshift galaxies. The ionization parameter can be determined with only UV lines, whereas the electron density and ISM pressure additionally require the [O II] λλ3727,9 doublet. We find the UV diagnostics used in this work alone cannot reliably constrain the electron temperature and oxygen abundance. This work paves the way for upcoming large telescopes (e.g. *JWST*, GMT, TMT, ELT) which will carry out rest-frame UV spectroscopic studies of galaxies out to redshifts exceeding 10.

REFERENCES

Aller L. H., ed., 1984, in Astrophysics and Space Science Library, Vol. 112, Physics of Thermal Gaseous Nebulae. Springer-Verlag, Berlin

Asplund M., Grevesse N., Sauval A. J., Scott P., 2009, ARA&A, 47, 481

Bayliss M. B., 2012, ApJ, 744, 156

Bayliss M. B., Rigby J. R., Sharon K., Wuyts E., Florian M., Gladders M. D., Johnson T., Oguri M., 2014, ApJ, 790, 144

Belfiore F. et al., 2017, MNRAS, 469, 151

Bian F., Kewley L. J., Dopita M. A., 2018, ApJ, 859, 175 (BKD18)

Bian F., Kewley L. J., Dopita M. A., Blanc G. A., 2017, ApJ, 834, 51

Bian F. et al., 2010, ApJ, 725, 1877

Blanc G. A., Kewley L., Vogt F. P. A., Dopita M. A., 2015, ApJ, 798, 99 (B15)

Bluck A. F. L., Mendel J. T., Ellison S. L., Moreno J., Simard L., Patton D. R., Starkenburg E., 2014, MNRAS, 441, 599

Bordoloi R., Rigby J. R., Tumlinson J., Bayliss M. B., Sharon K., Gladders M. G., Wuyts E., 2016, MNRAS, 458, 1891

Byler N., Dalcanton J. J., Conroy C., Johnson B. D., Levesque E. M., Berg D. A., 2018, ApJ, 863, 14

Cañameras R. et al., 2015, A&A, 581, A105

Cardelli J. A., Clayton G. C., Mathis J. S., 1989, ApJ, 345, 245

Christensen L. et al., 2012, MNRAS, 427, 1953

Cicone C., Maiolino R., Marconi A., 2016, A&A, 588, A41

Cicone C. et al., 2014, A&A, 562, A21

Contursi A. et al., 2017, A&A, 606, A86

D'Agostino J. J., Kewley L. J., Groves B., Byler N., Sutherland R. S., Nicholls D., Leitherer C., Stanway E. R., 2019, ApJ, 878, 2

Del Zanna G., Dere K. P., Young P. R., Landi E., Mason H. E., 2015, A&A, 582, A56

Dopita M. A. et al., 2006, ApJ, 647, 244

Dopita M. A., Sutherland R. S., Nicholls D. C., Kewley L. J., Vogt F. P. A., 2013, ApJS, 208, 10

Dopita M. A., Kewley L. J., Sutherland R. S., Nicholls D. C., 2016, Ap&SS, 361, 61(D16)

Ellison S. L., Sánchez S. F., Ibarra-Medel H., Antonio B., Mendel J. T., Barrera-Ballesteros J., 2018, MNRAS, 474, 2039

Erb D. K., Shapley A. E., Pettini M., Steidel C. C., Reddy N. A., Adelberger K. L., 2006, ApJ, 644, 813

Federrath C., Klessen R. S., 2012, ApJ, 761, 156

Federrath C. et al., 2017, in Crocker R. M., Longmore S. N., Bicknell G. V., eds, Proc. IAU Symp. Vol. 322, The Multi-Messenger Astrophysics of the Galactic Centre. Kluwer, Dordrecht, p. 123

Feltre A., Charlot S., Gutkin J., 2016, MNRAS, 456, 3354

Förster Schreiber N. M. et al., 2009, ApJ, 706, 1364

Gallazzi A., Charlot S., Brinchmann J., White S. D. M., Tremonti C. A., 2005, MNRAS, 362, 41

Gardner J. P. et al., 2006, Space Sci. Rev., 123, 485

Garnett D. R., Skillman E. D., Dufour R. J., Peimbert M., Torres-Peimbert S., Terlevich R., Terlevich E., Shields G. A., 1995a, ApJ, 443, 64

Garnett D. R., Dufour R. J., Peimbert M., Torres-Peimbert S., Shields G. A., Skillman E. D., Terlevich E., Terlevich R. J., 1995b, ApJ, 449, L77

Gilbank D. G., Gladders M. D., Yee H. K. C., Hsieh B. C., 2011, AJ, 141, 94

Groves B. A., Dopita M. A., Sutherland R. S., 2004, ApJS, 153, 9

Ho I.-T. et al., 2016, MNRAS, 457, 1257

Hook I., 2009, Astrophys. Space Sci. Proc., 9, 225

Izotov Y. I., Stasińska G., Meynet G., Guseva N. G., Thuan T. X., 2006a, A&A, 448, 955

Izotov Y. I., Papaderos P., Guseva N. G., Fricke K. J., Thuan T. X., 2006b, A&A, 454, 137

James B. L. et al., 2014, MNRAS, 440, 1794

James B. L., Auger M., Pettini M., Stark D. P., Belokurov V., Carniani S., 2018, MNRAS, 476, 1726

Jaskot A. E., Ravindranath S., 2016, ApJ, 833, 136

Johns M. W., 2004, in Ardeberg A. L., Andersen T., eds, Proc. SPIE Conf. Vol. 5382, Second Backaskog Workshop on Extremely Large Telescopes. SPIE, Bellingham, p. 85

Jones E. et al., 2001, SciPy: Open source scientific tools for Python. http://www.scipy.org/

Jones T., Ellis R., Jullo E., Richard J., 2010, ApJ, 725, L176

Jones T., Martin C., Cooper M. C., 2015, ApJ, 813, 126

Jones A. P., 2000, J. Geophys. Res., 105, 10257

Jones T. A., Ellis R. S., Schenker M. A., Stark D. P., 2013, ApJ, 779, 52

Kaasinen M., Bian F., Groves B., Kewley L. J., Gupta A., 2017, MNRAS, 465, 3220

Kaasinen M., Kewley L., Bian F., Groves B., Kashino D., Silverman J., Kartaltepe J., 2018, MNRAS, 477, 5568

Kennicutt Jr. R. C., 1984, ApJ, 287, 116

Kennicutt R. C. et al., 2011, PASP, 123, 1347

Kewley L. J., Dopita M. A., 2002, ApJS, 142, 35

Kewley L. J., Ellison S. L., 2008, ApJ, 681, 1183 (KE08)

Kewley L. J., Dopita M. A., Sutherland R. S., Heisler C. A., Trevena J., 2001, ApJ, 556, 121

Kewley L. J., Zahid H. J., Geller M. J., Dopita M. A., Hwang H. S., Fabricant D., 2015, ApJ, 812, L20

Kewley L. J. et al., 2016, ApJ, 819, 100

Kewley L. J. et al., 2019a, ApJ, in press (K19a)

Kewley L. J., Nicholls D. C., Sutherland R., 2019b, ARA&A, in press (K19b)

Kobulnicky H. A., Kewley L. J., 2004, ApJ, 617, 240

Kulas K., Shapley A., Hainline K., 2010, American Astronomical Society Meeting Abstracts #216. p. 417.08

Lamareille F., Mouhcine M., Contini T., Lewis I., Maddox S., 2004, MNRAS, 350, 396

Leethochawalit N., Jones T. A., Ellis R. S., Stark D. P., Zitrin A., 2016, ApJ, 831, 152

Leitherer C. et al., 1999, ApJS, 123, 3

Leitherer C., Tremonti C. A., Heckman T. M., Calzetti D., 2011, AJ, 141, 37

Leslie S. K., Kewley L. J., Sanders D. B., Lee N., 2016, MNRAS, 455, L82

Levesque E. M., Richardson M. L. A., 2014, ApJ, 780, 100

Lopez S. et al., 2018, Nature, 554, 493

López-Sánchez Á. R., Dopita M. A., Kewley L. J., Zahid H. J., Nicholls D. C., Scharwächter J., 2012, MNRAS, 426, 2630

Marshall J. L. et al., 2008, in McLean I. S., Casali M. M., eds, Proc. SPIE Conf. Ser. Vol. 7014, Ground-based and Airborne Instrumentation for Astronomy II. SPIE, Bellingham, p. 701454

McGaugh S. S., 1991, ApJ, 380, 140

McKinney W. R. et al., 2010, in Assoufid L., Takacs P. Z., Asundi A. K. eds , Proc. SPIE. Conf. Ser. Vol. 7801, Advances in Metrology for X-Ray and EUV Optics III. SPIE, Bellingham, p. 780106

McLean I. S. et al., 1998, in Fowler A. M., ed., Proc. SPIE Conf. Ser. Vol. 3354, Infrared Astronomical Instrumentation. SPIE, Bellingham, p. 566

Medling A. M. et al., 2018, MNRAS, 475, 5194

Osterbrock D. E., 1989, in Astrophysics of Gaseous Nebulae and Active Galactic Nuclei. University Science Books, Mill Valley, CA, USA

Pagel B. E. J., Edmunds M. G., Blackwell D. E., Chun M. S., Smith G., 1979, MNRAS, 189, 95

Pérez-Montero E., 2015, in Cenarro A. J., Figueras F., Hernández-Monteagudo C., Trujillo Bueno J., Valdivielso L., eds, Proc. XI Scientific Meeting of the Spanish Astronomical Society, Highlights of Spanish Astrophysics VIII. Teruel, Spain, p. 286

Pettini M., Pagel B. E. J., 2004, MNRAS, 348, L59

Prochaska J. X., Kasen D., Rubin K., 2011, ApJ, 734, 24

Richard J., Jones T., Ellis R., Stark D. P., Livermore R., Swinbank M., 2011, MNRAS, 413, 643

Rigby J., 2009, Resolved H Alpha Star Formation in Two Lensed Galaxies at z = 0.9, HST Proposal

Rigby J. R., Wuyts E., Gladders M. D., Sharon K., Becker G. D., 2011, ApJ, 732, 59

Rigby J. R., Bayliss M. B., Gladders M. D., Sharon K., Wuyts E., Dahle H., 2014, ApJ, 790, 44

Rigby J. R. et al., 2018, AJ, 155, 104

Sanders G. H., 2013, J. Astrophys. Astron., 34, 81

Sanders R. L. et al., 2016a, ApJ, 816, 23 (S16)

Sanders R. L. et al., 2016b, ApJ, 825, L23

Schneider D. P. et al., 1993, ApJS, 87, 45

Schulte-Ladbeck R. E., Miller C. J., Hopp U., Hopkins A., Nichol R. C., Voges W., Fang T., 2003, preprint (arxiv:astro-ph/0312069)

Schwamb M. E., Lintott C., Smethurst R., Kruk S., Matsushita S., Wong I., Wang S.-Y., 2016, American Astronomical Society Meeting Abstracts #227. p. 209.03

Shapley A. E., Erb D. K., Pettini M., Steidel C. C., Adelberger K. L., 2004, ApJ, 612, 108

Sharda P., Federrath C., da Cunha E., Swinbank A. M., Dye S., 2018, MNRAS, 477, 4380

Sharon K., Gladders M. D., Rigby J. R., Wuyts E., Koester B. P., Bayliss M. B., Barrientos L. F., 2012, ApJ, 746, 161

Shi F., Zhao G., Liang Y. C., 2007, A&A, 475, 409 (S07)

Stark D. P. et al., 2013, MNRAS, 436, 1040

Stark D. P. et al., 2014, MNRAS, 445, 3200

Stasińska G., 2002, in Henney W. J., Franco J., Martos M., eds, Revista Mexicana de Astronomia y Astrofisica Conference Series, Vol. 12. Mexico, p. 62

Steidel C. C. et al., 2014, ApJ, 795, 165

Stasińska G., 2005, A&A, 434, 507

Steidel C. C., Strom A. L., Pettini M., Rudie G. C., Reddy N. A., Trainor R. F., 2016, ApJ, 826, 159

Strom A. L., Steidel C. C., Rudie G. C., Trainor R. F., Pettini M., Reddy N. A., 2017, ApJ, 836, 164

Strom A. L., Steidel C. C., Rudie G. C., Trainor R. F., Pettini M., 2018, ApJ, 868, 117

Sutherland R., Dopita M., Binette L., Groves B., 2013, Astrophysics Source Code Library, record ascl:1306.008

Sutherland R. S., Dopita M. A., 1993, ApJS, 88, 253

Swinbank A. M. et al., 2015, ApJ, 806, L17

The Astropy Collaboration, 2013, A&A, 558, A33

Thomas A. D., Dopita M. A., Kewley L. J., Groves B. A., Sutherland R. S., Hopkins A. M., Blanc G. A., 2018, ApJ, 856, 89

Tremonti C. A. et al., 2004, ApJ, 613, 898

Uzgil B. D., Bradford C. M., Hailey-Dunsheath S., Maloney P. R., Aguirre J. E., 2016, ApJ, 832, 209

Vale Asari N., Stasińska G., Morisset C., Cid Fernandes R., 2016, MNRAS, 460, 1739

van Zee L., Haynes M. P., 2006, ApJ, 636, 214

Wang X. et al., 2017, ApJ, 837, 89

Whitaker K. E., Rigby J. R., Brammer G. B., Gladders M. D., Sharon K., Teng S. H., Wuyts E., 2014, ApJ, 790, 143(W14)

Wisnioski E. et al., 2015, ApJ, 799, 209

Wuyts E. et al., 2010, ApJ, 724, 1182

Wuyts E., Rigby J. R., Gladders M. D., Gilbank D. G., Sharon K., Gralla M. B., Bayliss M. B., 2012a, ApJ, 745, 86

Wuyts E., Rigby J. R., Sharon K., Gladders M. D., 2012b, ApJ, 755, 73

Wuyts E., Rigby J. R., Gladders M. D., Sharon K., 2014a, ApJ, 781, 61

Wuyts E. et al., 2014b, ApJ, 789, L40

Yuan T.-T., Kewley L. J., 2009, ApJ, 699, L161

Yuan T.-T., Kewley L. J., Richard J., 2013, ApJ, 763, 9

Yuan T.-T., Kewley L. J., Swinbank A. M., Richard J., Livermore R. C., 2011, ApJ, 732, L14

Zahid H. J., Kewley L. J., Bresolin F., 2011, ApJ, 730, 137

Zaritsky D., Kennicutt Jr. R. C., Huchra J. P., 1994, ApJ, 420, 87

Zhou L. et al., 2017, MNRAS, 470, 4573

APPENDIX A: ADDITIONAL IZIP ANALYSES

In this section we present the additional tests we conducted with IZIP. No user defined priors are used for these analyses in order to isolate the effects of the individual lines on the Bayesian estimates. Moreover, for computational efficiency, only 10 realizations (refer to Section 6) were performed for each of the cases discussed here, unlike the 100 realizations for those discussed before. Each test case
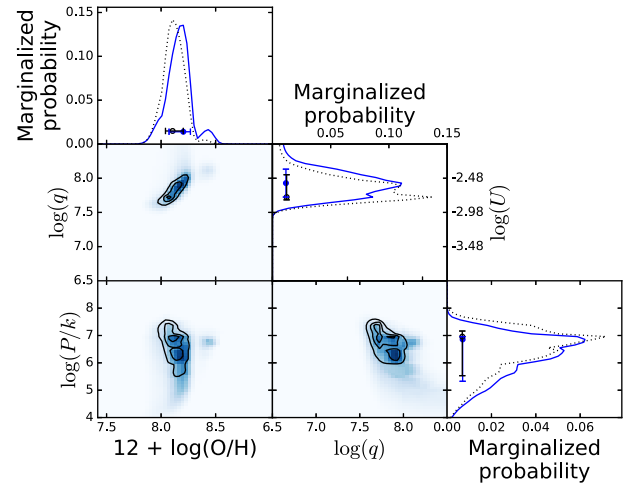
(a) All except [Si III]$\lambda\lambda$1882,92 lines used

Figure A1. Same as in Fig. 5 but here we investigate the effect of excluding the [Si III] $\lambda\lambda$1882,92 pair. The black contours and dotted histograms denote the fiducial case i.e. when all the lines are used. We assume flat prior in both these cases because the objective of this test was to isolate the effect of the [Si III] doublet. We find that log (q) is constained better on not using the [Si III] lines.
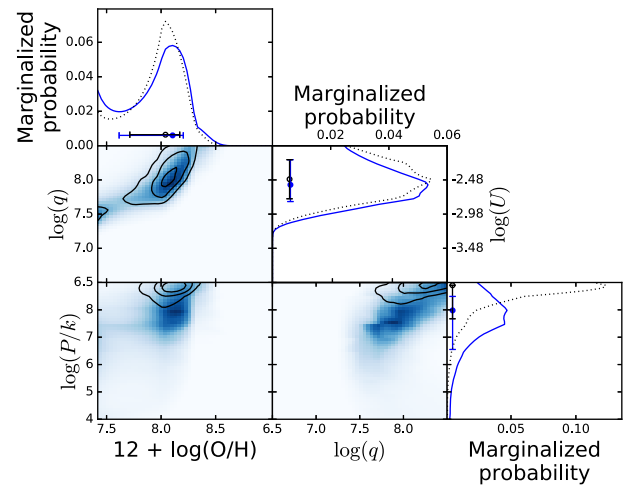
(a) All UV lines except [Si III]$\lambda\lambda$1882,92 used

Figure A2. Same as in Fig. 5 but this time using only the UV lines except the [Si III] $\lambda\lambda$1882,92 doublet. The black contours and dotted histograms denote the case all the UV lines are used. Similar to Fig. A1, we find that log (q) is constained better on excluding the [Si III] lines.

broadly converged by 10 realizations, and so our qualitative results and conclusions are robust.

We provide IZIP with the following different sets of emission lines to investigate the impact of the absence of a line or the presence of an additional line in determining the ISM properties. Please refer to Table 6 for the appropriate list of emission lines used.

(i) All the UV and optical emission lines *except* the [Si III] $\lambda\lambda$1882,92 doublet.

(ii) Only the UV lines except the [Si III] $\lambda\lambda$1882,92 doublet.

(iii) All the UV and optical emission lines *except* the [C III] $\lambda\lambda$1906,8 doublet.

(iv) Only the UV lines except the [C III] $\lambda\lambda$1906,8 doublet.

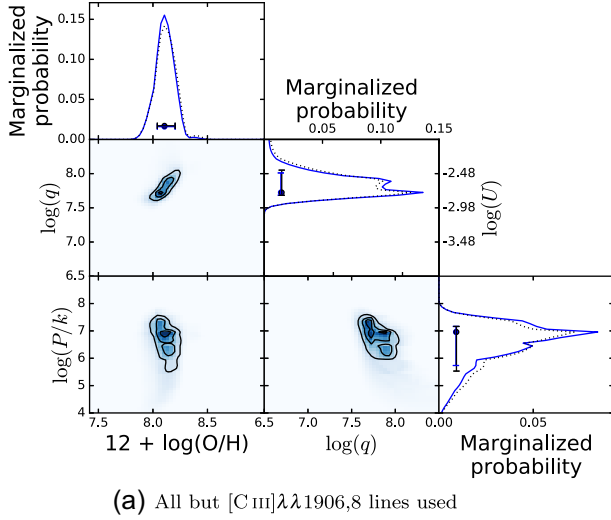**(a)** All but [C III]$\lambda\lambda$1906,8 lines used

Figure A3. Same as in Fig. 5 but this time without using all emission lines except [C III] $\lambda\lambda$1906,8. The black contours and dotted histograms denote the fiducial case i.e. when all the lines are used. Absence of [C III] does not have any discernible impact on any of the ISM properties.
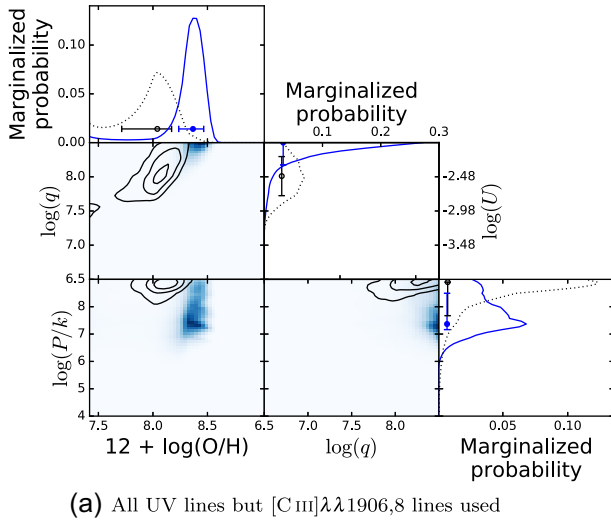

(a) All UV lines but [C III]$\lambda\lambda$1906,8 lines used

Figure A4. Same as in Fig. 5 but this time without using only UV emission lines except [C III] $\lambda\lambda$1906,8. The black contours and dotted histograms denote the case when all the UV lines are used. Although the $12 + \log(O/H)$ estimate is improved by dropping [C III], $\log(q)$ is now unconstrained.

(v) Only the UV lines and the H α line.
(vi) Only the UV lines and the H β line.
(vii) Only the UV lines along with the [O III] λ5007 line.

We also conduct tests with IZIP by providing only the emission lines sensitive to a single ISM parameter, at a time, as follows. We select the lines sensitive to a given ISM parameter as those used in the SEL diagnostics for that parameter (refer to Table 4).

(i) All emission lines (from Table 4) that are used for T_e diagnostic.
(ii) All emission lines (from Table 4) that are used for $12 + \log(O/H)$ diagnostic.
(iii) All emission lines (from Table 4) that are used for $\log(P/k)$ diagnostic.

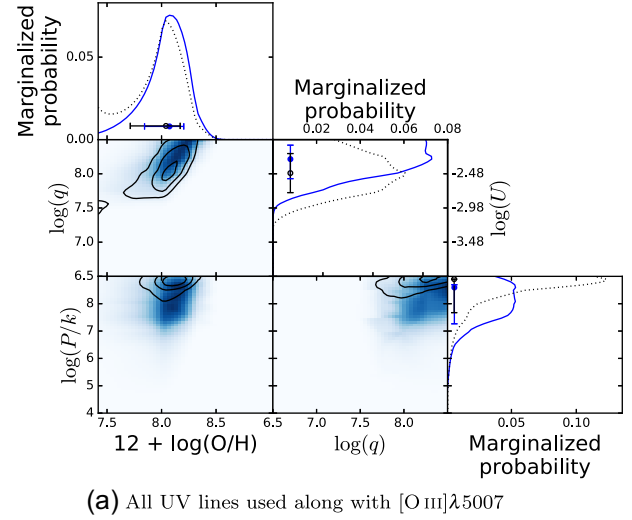**(a)** All UV lines used along with [O III]λ5007

Figure A5. Same as in Fig. 5 but this time using the [O III] λ5007 line along with rest-frame UV lines. The black contours and dotted histograms indicate the case when only the UV lines are used. Inclusion of [O III] helps to break the degeneracy of the metallicity branch, but fails to constrain $\log(q)$ or $\log(P/k)$.

(iv) All emission lines (from Table 4) that are used for $\log(q)$ diagnostic.

Figs A1–A7 show the results of the above tests and Table A1 quotes the corresponding values.

Exclusion of the [Si III] $\lambda\lambda$1882,92 lines from the UV–optical suite of emission lines constrains $\log(q)$ (Fig. A1) which otherwise hits the model grid boundaries. Depletion of Si from the gas phase on to dust grains or erosion of dust grains by shocks can have a considerable impact on the abundacne of Si in the ISM, which in turn may influence the [Si III] flux (Jones 2000). This is a potential source of discrepancy for diagnostics that use the [Si III] lines if the effects of dust have not been appropriately accounted for in the photoionization models (Byler et al. in preparation). However, excluding the [Si III] doublet from the set of UV lines (Fig. A2) makes the PDFs worse (compared to using all UV lines) i.e. $\log(q)$ now hits the model grid boundaries. This contradictory behaviour for UV–optical and only UV lines could be because the [Si III] doublet is one of the few SEL in the UV regime and removing it forces the Bayesian method to work with considerably less amount of information. Excluding the [Si III] $\lambda\lambda$1882,92 doublet makes very little difference to $\log(P/k)$ in either case (Figs A1 and A2) and yields a slightly lower ($\sim$0.3 dex) value of the inferred abundance but similar widths of the Z PDFs.

We find that absence of [C III] $\lambda\lambda$1906,8 does not impact the $\log(q)$ measurement when all lines are used (Fig. A3) but pushes it against the model grid ceiling when only rest-frame UV lines are used (Fig. A4). Such a dissimilarity exists because a considerably larger set of emission lines have been used in the former case than the latter, implying that the former configuration had more information available whereas the latter case did not have enough information to constrain the PDF. However, the abundance is much better constrained ($\sigma \sim 0.2$ dex) by only the UV lines on excluding [C III]. A similar effect is observed on including the [O III] λ5007 line with the UV lines (including [C III]), in that the oxygen abundance is better constrained but the $\log(q)$ and $\log(P/k)$ estimates fail. The $\log(q)$ and $\log(P/k)$ PDFs hit the model grid boundaries and we have tested
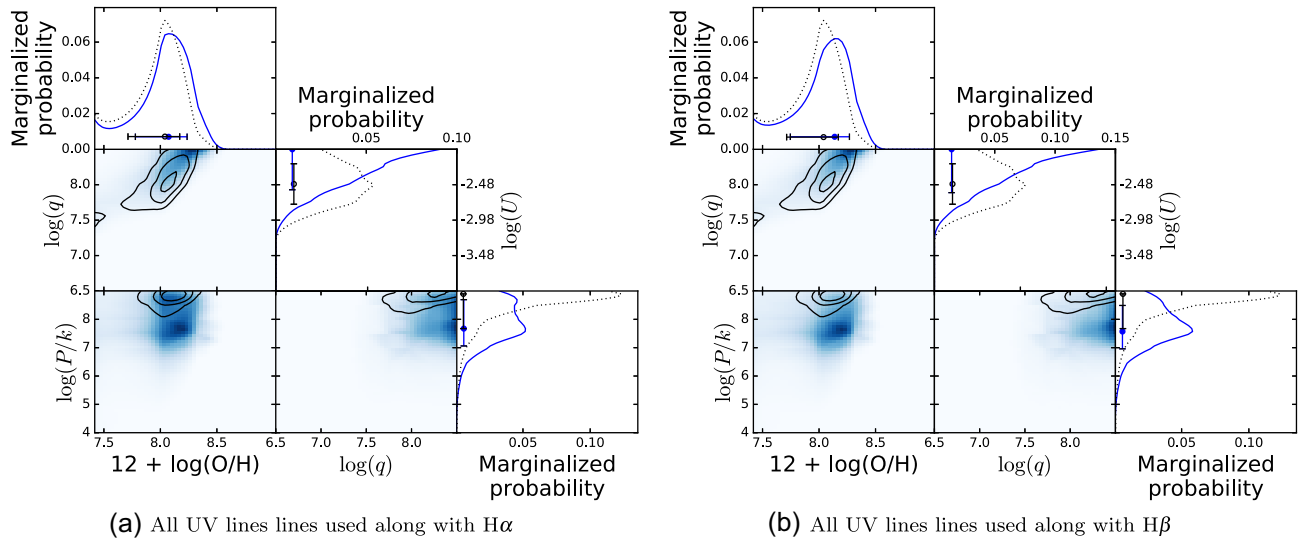
(a) All UV lines lines used along with Hα

(b) All UV lines lines used along with Hβ

Figure A6. Same as in Fig. 5 but this time without using only UV emission lines along with a Balmer line. Inclusion of Balmer lines does not have an appreciable impact on the metallicity constraints. Moreover, the $\log(q)$ and $\log(P/k)$ are unconstrained now, compared to when only UV lines were used (black contours and dotted histograms), thus suggesting that lack of Balmer lines in the UV spectra is not the main source of uncertainty.

Table A1. Inferred physical parameters by providing different sets of emission lines to *IZIP*. For computational efficiency, we performed only 10 realizations (refer to Section 6) for each of these cases (instead of 100, as in Table 5). However, each case was satisfactorily converged by then, and adding any more realization would not change the results qualitatively.

Lines provided to *IZIP*	Oxygen abundance $12 + \log(O/H)$	Ionization parameter $\log(q(\mathrm{cm\,s^{-1}}))$	ISM pressure $\log(P/k(\mathrm{K\,cm^{-3}}))$
All lines except [Si III] $\lambda\lambda 1882{,}92$	$8.20^{+0.07}_{-0.13}$	$7.93^{+0.20}_{-0.20}$	$6.86^{+0.10}_{-1.53}$
UV lines except [Si III] $\lambda\lambda 1882{,}92$	$8.11^{+0.10}_{-0.49}$	$7.93^{+0.37}_{-0.24}$	$7.98^{+0.51}_{-1.43}$
All lines except [C III] $\lambda\lambda 1906{,}8$	$8.11^{+0.1}_{-0.06}$	$7.72^{+0.29}_{-0.04}$	$6.96^{+0.20}_{-1.22}$
UV lines except [C III] $\lambda\lambda 1906{,}8$	$8.37^{+0.1}_{-0.13}$	Unconstrained	$7.37^{+1.22}_{-0.20}$
UV lines + H α	$8.07^{+0.16}_{-0.29}$	Unconstrained	$7.67^{+1.02}_{-0.61}$
UV lines + H β	$8.14^{+0.13}_{-0.39}$	Unconstrained	$7.57^{+0.92}_{-0.61}$
UV lines + [O III] $\lambda 5007$	$8.07^{+0.13}_{-0.23}$	Unconstrained	Unconstrained
All lines used for T_e diagnostic[a]	$8.24^{+0.16}_{-0.46}$	Unconstrained	Unconstrained
All lines used for $12 + \log(O/H)$ diagnostic[a]	$8.20^{+0.07}_{-0.1}$	$7.89^{+0.41}_{-0.12}$	$4.71^{+2.04}_{-0.20}$
All lines used for $\log(P/k)$ diagnostic[a]	Unconstrained	$7.85^{+0.45}_{-0.20}$	Unconstrained
All lines used for $\log(q)$ diagnostic[a]	$8.24^{+0.07}_{-0.23}$	$8.13^{+0.20}_{-0.24}$	$5.22^{+1.53}_{-0.41}$

[a]As per Table 4.

that simply extending the models towards higher values leads to unphysically high solutions for $\log(q)$ and $\log(P/k)$. The improved abundance estimate suggests that [O III is necessary to break the degeneracy in the metallicity branch, when using only UV lines.

Including Balmer lines with the UV spectra does not help improve the constraints. Similarly, providing *IZIP* with emission lines sensitive to one ISM parameter at a time, does not yield reliable estimates of the other parameters, or at times even the same

parameters which the input lines are sensitive to. This is because each parameter depends on the other and, in absence of spectral lines sensitive to the other two parameters, fails to reliably infer the concerned parameter as well. For instance, in Fig. A7(c), although only the lines sensitive to ISM pressure has been provided to *IZIP*, the absence of Z or $\log(q)$ sensitive lines leads to unconstrained Z and $\log(q)$ and consequently, fails to constrain $\log(P/k)$ which is dependent on the other two parameters.
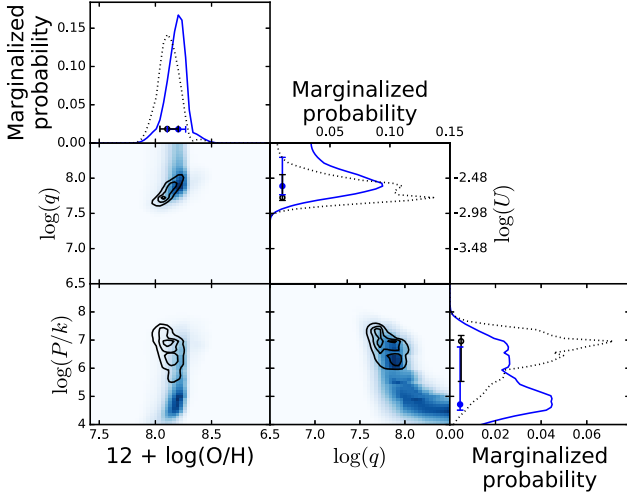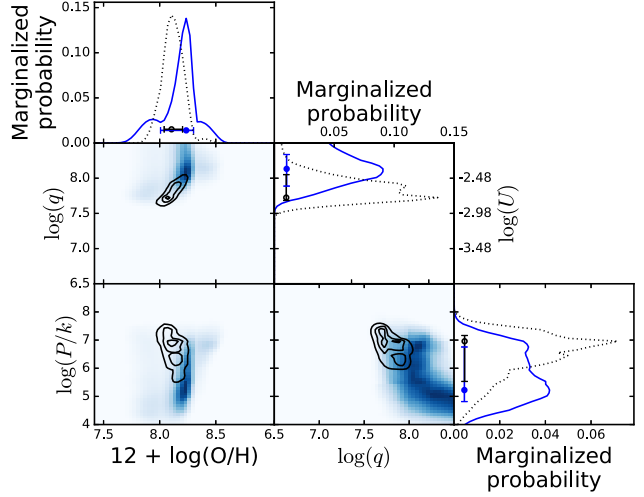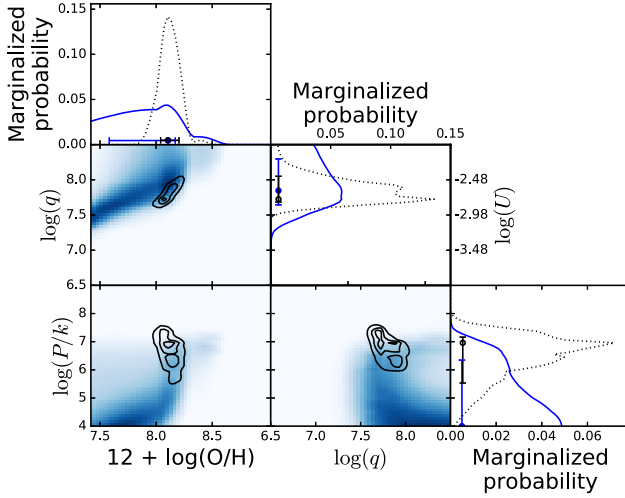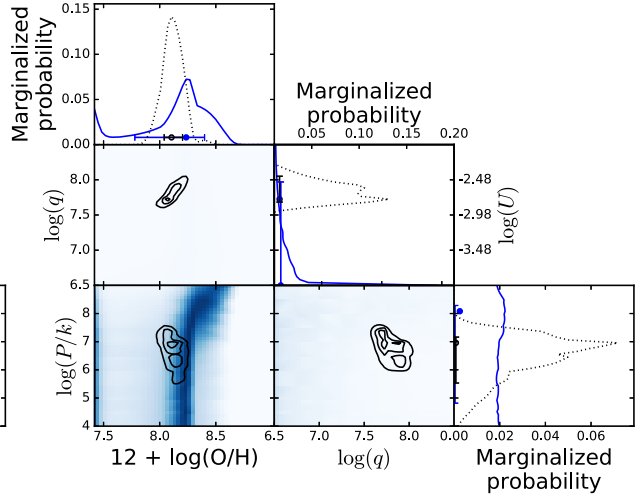
(a) Using all lines involved in SEL diagnostics for 12+log(O/H)

(b) Using all lines involved in SEL diagnostics for log(q)

(c) Using all lines involved in SEL diagnostics for log(P/k)

(d) Using all lines involved in SEL diagnostics for T_e

Figure A7. Same as in Fig. 5 but this time using only those emission lines that are sensitive to a specific ISM property. The black contours and dotted histograms represent the fiducial case i.e. when all the emission lines are used, without using a [N II]/Hα based prior. In none of these cases, are all three parameters well constrained. In the cases where only log(q) sensitive and only log(P/k) sensitive lines were provided, the respective parameters themselves are not constrained. We conclude that the parameters are interdependent and hence absence of the lines sensitive to one parameter leads to failure of the Bayesian estimate of another parameter even if the lines sensitive to the latter parameter is present. The only exception to this is when all metallicity sensitive lines are used, the metallicity and ionization parameter is well constrained. This is because the metallicity sensitive lines (in Table 4) already include the most of the (optical) log(q) sensitive lines.

This paper has been typeset from a TEX/LATEX file prepared by the author.